

Hydrodynamic interactions of spherical particles in suspensions confined between two planar walls.

By S. BHATTACHARYA,
J. BŁAWZDZIEWICZ, AND E. WAJNRYB†

Department of Mechanical Engineering, Yale University, New Haven, CT 06520-8286, USA

(Received)

Hydrodynamic interactions in a suspension of spherical particles confined between two parallel planar walls are studied under creeping-flow conditions. The many-particle friction matrix in this system is evaluated using our novel numerical algorithm based on transformations between Cartesian and spherical representations of Stokes flow. The Cartesian representation is used to describe the interaction of the fluid with the walls and the spherical representation is used to describe the interaction with the particles. The transformations between these two representations are given in a closed form, which allows us to evaluate the coefficients in linear equations for the induced-force multipoles on particle surfaces. The friction matrix is obtained from these equations, supplemented with the superposition lubrication corrections. We have used our algorithm to evaluate the friction matrix for a single sphere, a pair of spheres, and for linear chains of spheres. The friction matrix exhibits a crossover from a quasi-two-dimensional behavior (for systems with small wall separation H) to the three-dimensional behavior (when the distance H is much larger than the interparticle distance L). The crossover is especially pronounced for a long chain moving in the direction normal to its orientation and parallel to the walls. In this configuration, a large pressure buildup occurs in front of the chain for small values of the gapwidth H , which results in a large hydrodynamic friction force. A standard wall superposition approximation does not capture this behavior.

1. Introduction

Numerous recent papers reflect a growing interest in the static and dynamic properties of suspensions in confined geometries. There are investigations of the formation of colloidal crystals on patterned and planar surfaces (Lin *et al.* 2000; Seelig *et al.* 2002; Subramanian *et al.* 1999), studies of single-file diffusion of Brownian particles in a channel (Wei *et al.* 2000), and experiments on quasi-two-dimensional suspensions confined between two planar walls (Carbajal-Tinoco *et al.* 1997; Lançon *et al.* 2001; Marcus *et al.* 1999; Santana-Solano & Arauz-Lara 2001). Quasi-two-dimensional suspensions of particles adsorbed at a fluid interface (Zahn *et al.* 1997; Rinn *et al.* 1999; Cichocki *et al.* 2004) or confined in a thin liquid film (Sethumadhavan, Nikolov & Wasan 2001) have also been examined.

Experiments on quasi-two-dimensional systems revealed many striking phenomena like, for instance, the first-order transitions between fluid, hexatic, and solid phases (Marcus & Rice 1997), string-like cooperative motion of suspension particles (Marcus, Schofield & Rice

† On leave from IPPT Warsaw, Poland

1999), and oscillatory melting of a crystalline phase in shear flow (Stancik & Hawkinson 2003). Other interesting examples include a logarithmic behavior of the mean-square displacement of Brownian particles in quasi-two-dimensional systems, predicted by Cichocki & Felderhof (1994) and observed by Marcus *et al.* (1999); a hydrodynamic enhancement of self-diffusion for strongly-charged particles (Zahn *et al.* 1997; Pesché & Nägele 2000), and migration of particles in Poiseuille flow towards the channel center (Nott & Brady 1994; Lyon & Leal 1998).

The particle–wall and interparticle interaction potentials fully determine the equilibrium structure of confined colloidal suspensions. The dynamics of such systems, however, is significantly affected by the many-body hydrodynamic forces. For spherical particles in an unbounded space, efficient algorithms for evaluating many-body friction and mobility matrices have been developed (Durlafsky, Brady & Bossis 1987; Ladd 1988; Cichocki, Felderhof, Hinsén, Wajnryb & Bławdziewicz 1994; Sierou & Brady 2001). Using the image representation technique, such algorithms have been generalized for particles adsorbed on a planar fluid–air interface (Cichocki *et al.* 2004) and for particles confined in a thin liquid film (Bławdziewicz & Wajnryb 2003). The image-representation method has also been proposed for a suspension bounded by a single rigid planar wall (Cichocki & Jones 1998; Cichocki *et al.* 2000). A two-wall generalization of this method (Bhattacharya & Bławdziewicz 2002*a*) and several other techniques were used to describe motion of an individual particle between two planar walls (Ganatos *et al.* 1980*b,a*; Staben *et al.* 2003; Jones 2004).

The hydrodynamics of many particles in the two-wall geometry is much more complex, and available results are limited. Durlafsky & Brady (1989) have developed a method that combines boundary-integral and Stokesian-dynamics elements. In their approach, the walls are discretized, and the particles are represented using low-order force multipoles and lubrication contributions, as in the standard Stokesian-dynamics algorithm (Durlafsky *et al.* 1987). It seems that this method has not been further pursued. In an alternative approach, Nott & Brady (1994) and Morris & Brady (1998) studied flows in wall-bounded suspensions by modeling the walls as static, closely packed arrays of spheres, and using the standard Stokesian-dynamics algorithm for an unbounded system to evaluate the motion of the suspended particles. The results obtained in this way are only qualitative, especially for small wall separations, because the walls are porous and rough. Recently, a two-wall superposition approximation was used by Pesché & Nägele (2000) and several other groups, but the validity range of this approximation cannot be determined without comparison with more accurate results.

In our paper we present a novel, highly accurate algorithm to evaluate the many-body hydrodynamic interactions in a suspension of spherical particles confined between two planar walls. In our approach, the flow field in the system is expanded using two basis sets of solutions of Stokes equations—the spherical and Cartesian bases. The spherical basis is applied to describe the flow field scattered from the particles, and the Cartesian basis is used in the analysis of the interaction of the flow with the walls. The key result of our study is a set of transformation formulas for conversion between the spherical and Cartesian representations. In our algorithm the expansion of the flow field into the basis fields is combined with the two-particle superposition approximation for the friction matrix in order to incorporate slowly convergent lubrication corrections. Since the force multipoles induced on particle surfaces are included to arbitrary order, results of arbitrary accuracy are obtained.

Our paper is organized as follows. The induced-force formulation of the problem is described in §2, and the multipolar representation of the flow in terms of force multipoles induced on the particles is recalled in §3. Our main theoretical results are outlined in §4

and §5. The Cartesian basis set of Stokes flows is defined in §4, along with the transformation relations between the Cartesian and spherical bases, displacement theorems for the Cartesian basis fields and expressions for the wall-reflection matrix. These essential elements are combined in §5 to evaluate the wall contribution to the Green's matrix. The numerical implementation of our method is outlined in §6. Examples of numerical results (for a single particle, two particles and many-particle systems) are provided in §7. The multiparticle results have been selected to illustrate the crossover between the quasi-two-dimensional and three-dimensional behavior of the friction matrix as a function of the interparticle distance.

Since the full description of the theory underlying our algorithm requires more space, this paper outlines only the most important elements and lists the crucial results indispensable for the numerical implementation. The details of our theoretical analysis and a more complete description of the algorithm are presented in a separate publication (Bhattacharya *et al.* 2005), hereafter referred to as Ref. I.

2. Multiparticle hydrodynamic interactions

2.1. Hydrodynamic resistance

We consider a suspension of N spherical particles of the radius a in a creeping flow between two parallel planar walls. The no-slip boundary conditions are assumed on the particles and on the walls. The walls are at the positions $z = 0$ and $z = H$, where H is the separation between walls, and $\mathbf{r} = (x, y, z)$ are the Cartesian coordinates. The position of the center of particle i is denoted by $\mathbf{R}_i = (X_i, Y_i, Z_i)$, the translational and rotational particle velocities are denoted by \mathbf{U}_i and $\boldsymbol{\Omega}_i$, and the external forces and torques acting on the particle are denoted by \mathcal{F}_i and \mathcal{T}_i .

We focus on a system of spheres undergoing translational and rotational rigid-body motion with no external flow. As in an unbounded space, the particle dynamics in the system is characterized by the resistance matrix

$$\zeta_{ij} = \begin{bmatrix} \zeta_{ij}^{\text{tt}} & \zeta_{ij}^{\text{tr}} \\ \zeta_{ij}^{\text{rt}} & \zeta_{ij}^{\text{rr}} \end{bmatrix}, \quad i, j = 1, \dots, N, \quad (2.1)$$

defined by the linear relation

$$\begin{bmatrix} \mathcal{F}_i \\ \mathcal{T}_i \end{bmatrix} = \sum_{j=1}^N \begin{bmatrix} \zeta_{ij}^{\text{tt}} & \zeta_{ij}^{\text{tr}} \\ \zeta_{ij}^{\text{rt}} & \zeta_{ij}^{\text{rr}} \end{bmatrix} \cdot \begin{bmatrix} \mathbf{U}_j \\ \boldsymbol{\Omega}_j \end{bmatrix} \quad (2.2)$$

between the translational and rotational particle velocities and the forces and torques. The dot in equation (2.2) denotes the matrix multiplication and contraction of the Cartesian tensorial components of the resistance matrix.

2.2. Induced-force formulation

The effect of the suspended particles on the surrounding fluid can be described in terms of the induced force distributions on the particle surfaces

$$\mathbf{F}_i(\mathbf{r}) = a^{-2} \delta(r_i - a) \mathbf{f}_i(\mathbf{r}), \quad (2.3)$$

where

$$\mathbf{r}_i = \mathbf{r} - \mathbf{R}_i \quad (2.4)$$

and $r_i = |\mathbf{r}_i|$. By definition of the induced force, the flow field

$$\mathbf{v}(\mathbf{r}) = \sum_{i=1}^N \int \mathbf{T}(\mathbf{r}, \mathbf{r}') \cdot \mathbf{F}_i(\mathbf{r}') \, d\mathbf{r}' \quad (2.5)$$

is identical to the velocity field in the presence of the moving particles (Cox & Brenner 1967; Mazur & Bedeaux 1974; Felderhof 1976). Here

$$\mathbf{T}(\mathbf{r}, \mathbf{r}') = \mathbf{T}_0(\mathbf{r} - \mathbf{r}') + \mathbf{T}'(\mathbf{r}, \mathbf{r}') \quad (2.6)$$

is the Green's function for the Stokes flow in the presence of the boundaries; the Green's function $\mathbf{T}(\mathbf{r}, \mathbf{r}')$ is decomposed into the Oseen tensor $\mathbf{T}_0(\mathbf{r} - \mathbf{r}')$ and the part $\mathbf{T}'(\mathbf{r}, \mathbf{r}')$ that describes the flow reflected from the walls. In equation (2.5) it is assumed that the particles move with given velocities, but no external flow is imposed.

The resistance relation (2.2) is linked to the induced-force distributions (2.3) through the expressions

$$\mathcal{F}_i = \int \mathbf{F}_i(\mathbf{r}) \, d\mathbf{r}, \quad \mathcal{T}_i = \int \mathbf{r}_i \times \mathbf{F}_i(\mathbf{r}) \, d\mathbf{r} \quad (2.7)$$

for the total force and torque, respectively. To determine the resistance matrix (2.1) we thus need to evaluate the induced forces (2.3) for given translational and angular velocities of the particles.

2.3. Boundary-integral equations for the induced forces

For a system of particles moving with the translational and angular velocities \mathbf{U}_i and $\mathbf{\Omega}_i$, the induced-force distribution (2.3) can be obtained from the boundary-integral equation of the form

$$[\mathbf{Z}_i^{-1} \mathbf{F}_i](\mathbf{r}) + \sum_{j=1}^N \int [(1 - \delta_{ij}) \mathbf{T}_0(\mathbf{r} - \mathbf{r}') + \mathbf{T}'(\mathbf{r}, \mathbf{r}')] \cdot \mathbf{F}_j(\mathbf{r}') \, d\mathbf{r}' = \mathbf{v}_i^{\text{rb}}(\mathbf{r}), \quad \mathbf{r} \in S_i, \quad (2.8)$$

where

$$\mathbf{v}_i^{\text{rb}}(\mathbf{r}) = \mathbf{U}_i + \mathbf{\Omega}_i \times \mathbf{r}_i \quad (2.9)$$

is the rigid-body velocity field associated with the particle motion, and S_i is the surface of particle i . In the boundary-integral equation (2.8), \mathbf{Z}_i denotes the one-particle scattering operator that describes the response of an individual particle to an external flow in an unbounded space. This operator is defined by the linear relation

$$\mathbf{F}_i = -\mathbf{Z}_i(\mathbf{v}_i^{\text{in}} - \mathbf{v}_i^{\text{rb}}), \quad (2.10)$$

where \mathbf{v}_i^{in} is the velocity incident to particle i . For specific particle models, explicit expressions for the operator \mathbf{Z}_i are known (Jones & Schmitz 1988; Cichocki *et al.* 1988; Bławdziewicz *et al.* 1999).

3. Force-multipole expansion

3.1. Spherical basis fields

As in a standard force-multipole approach (Cichocki *et al.* 1994, 2000) the boundary-integral equation (2.8) is transformed into a linear matrix equation by projecting it onto a spherical basis of Stokes flow. To this end we use the reciprocal basis sets defined by Cichocki *et al.* (1988); we introduce, however, a slightly different normalization to exploit the full symmetry of the problem.

The singular and nonsingular spherical basis solutions of Stokes equations $\mathbf{v}_{lm\sigma}^-(\mathbf{r})$ and $\mathbf{v}_{lm\sigma}^+(\mathbf{r})$ (with $l = 1, 2, \dots$; $m = -l, \dots, l$; and $\sigma = 0, 1, 2$) have the following separable form in the spherical coordinates $\mathbf{r} = (r, \theta, \phi)$:

$$\mathbf{v}_{lm\sigma}^-(\mathbf{r}) = \mathbf{V}_{lm\sigma}^-(\theta, \phi)r^{-(l+\sigma)}, \quad (3.1a)$$

$$\mathbf{v}_{lm\sigma}^+(\mathbf{r}) = \mathbf{V}_{lm\sigma}^+(\theta, \phi)r^{l+\sigma-1}, \quad (3.1b)$$

where the coefficients $\mathbf{V}_{lm\sigma}^-(\theta, \phi)$ and $\mathbf{V}_{lm\sigma}^+(\theta, \phi)$ are combinations of vector spherical harmonics with angular order l and azimuthal order m . This property and the r -dependence in equations (3.1) define the Stokes-flow fields $\mathbf{v}_{lm\sigma}^\pm(\mathbf{r})$ up to a normalization constant. Explicit expressions for the functions $\mathbf{V}_{lm\sigma}^\pm$ in our present normalization are given in Appendix A. The justification for this choice of the normalization is discussed in Ref. I.

Following Cichocki *et al.* (1988) we also introduce the reciprocal basis fields $\mathbf{w}_{lm\sigma}^\pm(\mathbf{r})$, defined here by the orthogonality relations of the form

$$\langle \delta_a^S \mathbf{w}_{lm\sigma}^\pm | \mathbf{v}_{l'm'\sigma'}^\pm \rangle = \delta_{ll'} \delta_{mm'} \delta_{\sigma\sigma'}, \quad (3.2)$$

where

$$\delta_a^S(\mathbf{r}) = a^{-2} \delta(r - a), \quad (3.3)$$

and

$$\langle \mathbf{A} | \mathbf{B} \rangle = \int \mathbf{A}^*(\mathbf{r}) \cdot \mathbf{B}(\mathbf{r}) \, d\mathbf{r}. \quad (3.4)$$

The asterisk in the above relation denotes the complex conjugate. We note that due to the proper choice of defining properties of the spherical basis sets, the basis fields $\mathbf{v}_{lm\sigma}^-$ and $\mathbf{w}_{lm\sigma}^+$ satisfy relation (Cichocki *et al.* 1988)

$$\mathbf{v}_{lm\sigma}^-(\mathbf{r}) = \eta \int \mathbf{T}_0(\mathbf{r} - \mathbf{r}') \delta_a^S(\mathbf{r}') \mathbf{w}_{lm\sigma}^+(\mathbf{r}') \, d\mathbf{r}', \quad (3.5)$$

where η is the viscosity of the fluid. Relation (3.5) assures that the Lorentz reciprocal symmetry of Stokes flow is reflected in the symmetry of the resulting matrix representation of the problem (Cichocki *et al.* 2000).

3.2. Matrix representation

The matrix representation of the boundary-integral equation (2.8) is obtained by expanding the force distributions induced on each particle into the induced-force multipoles. The force multipolar moments of the force distribution (2.3) are defined by the relation

$$\mathbf{F}_i(\mathbf{r}) = \sum_{lm\sigma} f_i(lm\sigma) a^{-2} \delta(r_i - a) \mathbf{w}_{lm\sigma}^+(\mathbf{r}_i), \quad (3.6)$$

where \mathbf{r}_i is the relative position (2.4) with respect to the particle center. According to equations (3.5) and (3.6), the multipolar moments $f_i(lm\sigma)$ are identical (apart from the trivial factor η) to the expansion coefficients of the flow field scattered by an isolated particle in unbounded space into the singular basis fields $\mathbf{v}_{lm\sigma}^-$.

To obtain a linear matrix equation for the set of force multipolar moments $f_i(lm\sigma)$, the multipolar representation of the induced force (3.6) is inserted into the boundary-integral equation (2.8), and the resulting expression is expanded into the nonsingular basis solutions (3.1b). In particular, for the rigid-body velocity field we have

$$\mathbf{v}_i^{\text{rb}}(\mathbf{r}) = \sum_{lm\sigma} c_i(lm\sigma) \mathbf{v}_{lm\sigma}^+(\mathbf{r}_i), \quad (3.7)$$

where the expansion coefficients $c_i(lm\sigma)$ are nonzero only for $l = 1$ and $\sigma = 0, 1$.

As the result of this procedure we get the linear force-multipole equation, which can be written in the form

$$\sum_{j=1}^N \sum_{l'm'} \mathbf{M}_{ij}(lm | l'm') \cdot \mathbf{f}_j(l'm') = \mathbf{c}_i(lm). \quad (3.8)$$

We use here a matrix notation in the three-dimensional linear space with the components corresponding to the indices $\sigma = 0, 1, 2$ that identify the tensorial character of the basis flow fields (3.1). Accordingly, the arrays $\mathbf{f}_j(l'm')$ and $\mathbf{c}_i(lm)$ have the components $f_j(l'm'\sigma')$ and $c_i(lm\sigma)$ and the matrix $\mathbf{M}_{ij}(lm | l'm')$ has the elements $M_{ij}(lm\sigma | l'm'\sigma')$, where $\sigma, \sigma' = 0, 1, 2$. The many-particle resistance matrix (2.1) can be obtained by solving equation (3.8) and projecting the induced force multipoles onto the total force and torque (2.7). Explicit expressions for the resistance matrix in terms of the generalized friction matrix $\mathbf{F} = \mathbf{M}^{-1}$ are given in Appendix B.

For a wall bounded system the matrix \mathbf{M} can be decomposed into three contributions

$$\mathbf{M}_{ij}(lm | l'm') = \delta_{ij} \delta_{ll'} \delta_{mm'} \mathbf{Z}_i^{-1}(l) + \mathbf{G}_{ij}^0(lm | l'm') + \mathbf{G}'_{ij}(lm | l'm'). \quad (3.9)$$

The first term $\mathbf{Z}_i^{-1}(l)$ corresponds to the one particle operator \mathbf{Z}_i^{-1} in equation (2.8). Accordingly, the matrix $\mathbf{Z}_i(l)$ relates the force multipoles $\mathbf{f}_i(l'm')$ induced on particle i to the coefficients in the expansion of the flow field incoming to this particle into the nonsingular spherical basis fields (3.1b). By spherical symmetry, this term is diagonal in the multipolar orders l and m , and for rigid spheres it is explicitly known (Cichocki *et al.* 1988).

The Green matrices $\mathbf{G}_{ij}^0(lm | l'm')$ and $\mathbf{G}'_{ij}(lm | l'm')$ correspond to the integral operators with the kernels $\mathbf{T}_0(\mathbf{r} - \mathbf{r}')$ and $\mathbf{T}'(\mathbf{r}, \mathbf{r}')$ in equation (2.8). As discussed by Cichocki *et al.* (2000) and by Bhattacharya *et al.* (2005) the matrix $\mathbf{G}_{ij}^0(lm | l'm')$ coincides (apart from the normalization factors) with the displacement matrix for spherical basis fields, which is explicitly known (Felderhof & Jones 1989). The only unknown component in expression (3.9) is thus the wall contribution

$$G'_{ij}(lm\sigma | l'm'\sigma') = \langle \delta_a^S(\mathbf{r}_i) \mathbf{w}_{lm\sigma}^+(\mathbf{r}_i) | \mathbf{v}'_{l'm'\sigma'}(\mathbf{r}_j) \rangle, \quad (3.10)$$

where

$$\mathbf{v}'_{l'm'\sigma'}(\mathbf{r}) = \int \mathbf{T}'(\mathbf{r}, \mathbf{r}') \delta_a^S(\mathbf{r}') \mathbf{w}_{l'm'\sigma'}^+(\mathbf{r}') d\mathbf{r}'. \quad (3.11)$$

In the following sections we express this contribution in terms of the Cartesian basis set of Stokes flows.

4. Cartesian representation

The difficulties associated with the evaluation of the matrix \mathbf{G}'_{ij} in systems with two planar walls stem from the incompatibility of the spherical basis fields $\mathbf{v}_{lm\sigma}^\pm$ with the wall geometry. In particular, the image representation of a force multipole (Cichocki & Jones 1998; Bhattacharya & Bławdziewicz 2002a) is insufficient for a two-wall system, due to the slow convergence of the multiple-image series. We propose here an alternative technique, which relies on a transformation between the spherical basis fields (3.1) and a Cartesian basis set of Stokes flows. In the Cartesian representation the flow reflected from the walls can be obtained in a closed form; thus the difficulties associated with the multiple-image series are avoided.

According to our Cartesian representation method, the wall contribution (3.10) to

the matrix \mathbf{M} is evaluated by (i) expanding the spherical basis flow field $\mathbf{v}_{l'm'\sigma'}^-(\mathbf{r}_j)$ produced by a force multipole at the position \mathbf{r}_j into the Cartesian basis; (ii) solving the two-wall problem in the Cartesian representation; and (iii) transforming the resulting reflected flow back to the spherical basis (3.1b) centered at the position \mathbf{r}_i . As a result of this procedure, the matrix elements (3.10) are expressed in terms of two-dimensional Fourier integrals with respect to the lateral coordinates x, y . Our method is outlined in the following sections.

4.1. Cartesian basis

To describe the flow field between two walls parallel to the x - y plane, it is convenient to use a basis set of Stokes flows of the separable form

$$\mathbf{v}_{\mathbf{k}\sigma}^\pm(\mathbf{r}) = \mathbf{V}_{\mathbf{k}\sigma}^\pm(z) e^{i\mathbf{k}\cdot\rho \pm kz} \quad (4.1)$$

that is consistent with the wall geometry. Here

$$\boldsymbol{\rho} = x\hat{\mathbf{e}}_x + y\hat{\mathbf{e}}_y \quad (4.2)$$

is the projection of the vector \mathbf{r} onto the x - y plane,

$$\mathbf{k} = k_x\hat{\mathbf{e}}_x + k_y\hat{\mathbf{e}}_y \quad (4.3)$$

is the corresponding two-dimensional wave vector, and $k = |\mathbf{k}|$. By analogy to the spherical basis (3.1), there exist three types of solutions $\sigma = 0, 1, 2$ for each \mathbf{k} . These solutions involve a potential flow, a flow with nonzero vorticity, and a pressure-driven flow. Explicit expressions for the coefficients $\mathbf{V}_{\mathbf{k}\sigma}^\pm(z)$ are given in Appendix C. To achieve a substantial simplification of our final results, the relative amplitudes of the three components in the basis fields (4.1) have been carefully chosen, as discussed in Ref. I.

4.2. Transformation relations

The transformation relations between the spherical and Cartesian sets of solutions of Stokes equations can be expressed by the formulas

$$\mathbf{v}_{lm\sigma}^- = \int d\mathbf{k}' \sum_{\sigma'} \mathbf{v}_{\mathbf{k}'\sigma'}^\pm(\mathbf{r}) T_{\text{CS}}^{\pm-}(\mathbf{k}', lm; \sigma' | \sigma), \quad \pm z < 0, \quad (4.4)$$

$$\mathbf{v}_{\mathbf{k}\sigma}^\pm(\mathbf{r}) = \sum_{l'm'\sigma'} \mathbf{v}_{l'm'\sigma'}^\pm(\mathbf{r}) T_{\text{SC}}^{\pm\pm}(l'm', \mathbf{k}; \sigma' | \sigma). \quad (4.5)$$

As demonstrated in Ref. I, the transformation matrices $\mathbf{T}_{\text{CS}}^{\pm-}(\mathbf{k}, lm)$ and $\mathbf{T}_{\text{SC}}^{\pm\pm}(lm, \mathbf{k})$ have the factorized form

$$\mathbf{T}_{\text{SC}}^{\pm\pm}(lm, \mathbf{k}) = (-i)^m (2\pi k)^{-1/2} e^{-im\psi} \mathbf{K}(k, l) \cdot \tilde{\mathbf{T}}_{\text{SC}}^{\pm\pm}(lm), \quad (4.6a)$$

$$\mathbf{T}_{\text{CS}}^{\pm-}(\mathbf{k}, lm) = i^m (2\pi k)^{-1/2} e^{im\psi} \tilde{\mathbf{T}}_{\text{CS}}^{\pm-}(lm) \cdot \mathbf{K}(k, l), \quad (4.6b)$$

where ψ is the polar angle in the Fourier space,

$$K(k, l; \sigma | \sigma') = \delta_{\sigma\sigma'} k^{l+\sigma-1}, \quad (4.7)$$

and the matrices $\tilde{\mathbf{T}}_{\text{SC}}^{\pm\pm}(lm)$ and $\tilde{\mathbf{T}}_{\text{CS}}^{\pm-}(lm)$ are independent of the wave vector \mathbf{k} . Due to the proper choice of the spherical and Cartesian fields, the transformation matrices

$\tilde{\mathbf{T}}_{\text{SC}}^{\pm\pm}(lm)$ and $\tilde{\mathbf{T}}_{\text{CS}}^{\pm\pm}(lm)$ have a simple symmetric form

$$\tilde{\mathbf{T}}_{\text{SC}}^{++} = [\tilde{\mathbf{T}}_{\text{SC}}^{--}]^\dagger = \begin{bmatrix} a & b & c \\ 0 & 2a & 2b \\ 0 & 0 & 4a \end{bmatrix}, \quad (4.8a)$$

$$\tilde{\mathbf{T}}_{\text{SC}}^{+-} = [\tilde{\mathbf{T}}_{\text{CS}}^{+-}]^\dagger = (-1)^{l+m} \begin{bmatrix} c & b & a \\ -2b & -2a & 0 \\ 4a & 0 & 0 \end{bmatrix}, \quad (4.8b)$$

where the dagger denotes the Hermitian conjugate. The three independent scalar coefficients in equations (4.8) are

$$a = [4(l-m)!(l+m)!(2l+1)]^{-1/2}, \quad (4.9a)$$

$$b = 2am/l, \quad (4.9b)$$

$$c = a \frac{l(2l^2 - 2l - 1) - 2m^2(l-2)}{l(2l-1)}. \quad (4.9c)$$

4.3. Cartesian displacement formulas

In an analysis of the flow between the walls it is convenient to use the Cartesian basis fields centered at different positions (e.g., the particle or wall position). As shown in Ref. I, the fields (4.1) centered at different points \mathbf{R}_1 and \mathbf{R}_2 are related by the displacement formula

$$\mathbf{v}_{\mathbf{k}\sigma}^\pm(\mathbf{r}_2) = \sum_{\sigma'} \mathbf{v}_{\mathbf{k}\sigma'}^\pm(\mathbf{r}_1) S_C^{\pm\pm}(\mathbf{R}_{12}, \mathbf{k}; \sigma' | \sigma), \quad (4.10)$$

where $\mathbf{r}_1 = \mathbf{r} - \mathbf{R}_1$, $\mathbf{r}_2 = \mathbf{r} - \mathbf{R}_2$, and $\mathbf{R}_{12} = \mathbf{R}_1 - \mathbf{R}_2$. Since the shift of the origin of the coordinate system preserves the behavior of the flow fields (4.1) at infinity, the superscripts in equation (4.10) are either all positive or all negative. The displacement matrices $\mathbf{S}_C^{\pm\pm}(\mathbf{R}_{12}, \mathbf{k})$ can be factorized as follows,

$$\mathbf{S}_C^{\pm\pm}(\mathbf{R}_{12}, \mathbf{k}) = \tilde{\mathbf{S}}_C^{\pm\pm}(kZ_{12}) e^{i\mathbf{k} \cdot \boldsymbol{\rho}_{12}}, \quad (4.11)$$

where

$$\tilde{\mathbf{S}}_C^{--}(kZ) = \begin{bmatrix} 1 & 0 & 0 \\ 0 & 1 & 0 \\ -2kZ & 0 & 1 \end{bmatrix} e^{-kZ}, \quad \tilde{\mathbf{S}}_C^{++}(kZ) = \begin{bmatrix} 1 & 0 & 2kZ \\ 0 & 1 & 0 \\ 0 & 0 & 1 \end{bmatrix} e^{kZ}, \quad (4.12)$$

and

$$\mathbf{R}_{12} = \boldsymbol{\rho}_{12} + Z_{12} \hat{\mathbf{e}}_z. \quad (4.13)$$

4.4. Single-wall reflection matrix

The Cartesian basis fields (4.1) are well suited for a description of the interaction of the flow with planar walls because, due to the translational invariance of the problem, the lateral Fourier modes with different wave vectors \mathbf{k} do not couple. The effect of a single wall on the flow field in the system can be characterized in terms of the one-wall reflection matrix \mathbf{Z}_w . To define this quantity we consider Stokes flow in a fluid bounded by a single wall in the plane

$$z = Z_w. \quad (4.14)$$

The fluid occupies either the halfspace $z > Z_w$ (denoted by Ω^+) or $z < Z_w$ (denoted by Ω^-).

The velocity field in the halfspace Ω^\pm can be uniquely decomposed into the incoming and reflected flows

$$\mathbf{v}(\mathbf{r}) = \mathbf{v}_w^{\text{in}}(\mathbf{r}) + \mathbf{v}_w^{\text{out}}(\mathbf{r}). \quad (4.15)$$

The flow $\mathbf{v}_w^{\text{in}}(\mathbf{r})$ is nonsingular in the halfspace Ω^\mp , and the flow $\mathbf{v}_w^{\text{out}}(\mathbf{r})$ is nonsingular in the halfspace Ω^\pm . Thus these flows have the following expansions in the Cartesian basis,

$$\mathbf{v}_w^{\text{in}}(\mathbf{r}) = \int d\mathbf{k} \sum_{\sigma} c_w^{\text{in}}(\mathbf{k}\sigma) \mathbf{v}_{\mathbf{k}\sigma}^{\pm}(\mathbf{r}_w), \quad (4.16a)$$

$$\mathbf{v}_w^{\text{out}}(\mathbf{r}) = \int d\mathbf{k} \sum_{\sigma} c_w^{\text{out}}(\mathbf{k}\sigma) \mathbf{v}_{\mathbf{k}\sigma}^{\mp}(\mathbf{r}_w). \quad (4.16b)$$

Here

$$\mathbf{r}_w = \mathbf{r} - \mathbf{R}_w \quad (4.17)$$

denotes the position of the point \mathbf{r} relative to the wall, where $\mathbf{R}_w = (X_w, Y_w, Z_w)$ has arbitrary lateral coordinates X_w and Y_w .

The single-wall scattering matrix \mathbf{Z}_w relates the expansion coefficients of the incoming and reflected flows:

$$\mathbf{c}_w^{\text{out}}(\mathbf{k}) = -\mathbf{Z}_w \cdot \mathbf{c}_w^{\text{in}}(\mathbf{k}), \quad (4.18)$$

where $\mathbf{c}_w^{\text{out}}(\mathbf{k})$ and $\mathbf{c}_w^{\text{in}}(\mathbf{k})$ denote the arrays of expansion coefficients in equations (4.16). For a rigid wall with no-slip boundary conditions we have

$$\mathbf{Z}_w = \begin{bmatrix} 1 & 0 & 0 \\ 0 & 1 & 0 \\ 0 & 0 & 1 \end{bmatrix}, \quad (4.19)$$

as shown in Ref. I. For planar interfaces with other boundary conditions (e.g., a surfactant-covered fluid-fluid interface discussed by Bławdziewicz, Cristini & Loewenberg 1999) the scattering matrix can also be obtained.

5. Evaluation of the wall contribution to Green's matrix

5.1. Single-wall system

The transformation, displacement, and reflection matrices described in §4 can be used to construct the matrix \mathbf{G}'_{ij} for a suspension bounded by a single planar wall or by two planar walls. For a single wall, the matrix (3.10) can be expressed by the two-dimensional Fourier integral

$$\mathbf{G}'_{ij}(lm | l'm') = \int d\mathbf{k} \tilde{\Psi}_s(\mathbf{k}; Z_{iw}, Z_{wj}) e^{i\mathbf{k} \cdot \boldsymbol{\rho}_{ij}} \quad (5.1)$$

with the integrand of the form

$$\tilde{\Psi}_s(\mathbf{k}; Z_{iw}, Z_{wj}) = -\eta^{-1} \mathbf{T}_{\text{SC}}^{+\mp}(\mathbf{k}, lm) \cdot \tilde{\mathbf{S}}_{\text{C}}^{\mp\mp}(kZ_{iw}) \cdot \mathbf{Z}_w \cdot \tilde{\mathbf{S}}_{\text{C}}^{\pm\pm}(kZ_{wj}) \cdot \mathbf{T}_{\text{CS}}^{\pm-}(\mathbf{k}, l'm'), \quad (5.2)$$

where $Z_{iw} = Z_i - Z_w$ and $Z_{wj} = Z_w - Z_j$ are the vertical offsets between the points i and j and the wall.

The physical interpretation of relation (5.2) is straightforward. First, the spherical components of the flow produced by a multipolar force distribution at point j are transformed by the matrix $\mathbf{T}_{\text{CS}}^{\pm-}$ into the Cartesian basis. The Cartesian components of the

velocity field are propagated by the matrix $\mathbf{S}_C^{\pm\pm}(\mathbf{R}_{wj})$ to the wall, where they are scattered, as represented by the matrix \mathbf{Z}_w . The reflected field is propagated by the matrix $\mathbf{S}_C^{\mp\mp}(\mathbf{R}_{iw})$ to the point i , and, finally, the flow is transformed by the matrix $\mathbf{T}_{SC}^{\pm\mp}$ back into the spherical basis.

Due to symmetry properties of the component matrices (cf., relations (4.6), (4.8), (4.12), and (4.19)) the wall contribution to the Green's matrix (5.1) satisfies the Lorentz symmetry

$$\mathbf{G}'_{ij}(lm | l'm') = \mathbf{G}'_{ji}{}^\dagger(l'm' | lm). \quad (5.3)$$

We note that for the single-wall problem the Fourier integral (5.1) can be explicitly performed, which yields the image-singularity result derived by Cichocki & Jones (1998). As discussed in §6, both the Fourier representation (5.1) and the result of Cichocki & Jones (1998) are used in our algorithm to accelerate the convergence of the two-wall integrals by a subtraction of the single-wall contributions.

5.2. Two-wall system

The single-wall result presented above can be generalized to the flow between two parallel walls. We assume that the walls are in the planes

$$z = Z_L, \quad z = Z_U, \quad (5.4)$$

where

$$Z_L < Z_U. \quad (5.5)$$

The two-wall Green's matrix (3.10) can be expressed in the form analogous to equations (5.1) and (5.2), i.e.,

$$\mathbf{G}'_{ij}(lm | l'm') = \int d\mathbf{k} \tilde{\Psi}(\mathbf{k}; Z_{iL}, Z_{jL}, Z_{LU}) e^{i\mathbf{k} \cdot \boldsymbol{\rho}_{ij}}, \quad (5.6)$$

$$\tilde{\Psi}(\mathbf{k}; Z_{iL}, Z_{jL}, Z_{LU}) = -\eta^{-1} T_{SC}(lm, \mathbf{k}) \cdot \tilde{\mathbf{S}}_{iW}(\mathbf{k}) \cdot \tilde{\mathbf{Z}}_{TW}(\mathbf{k}) \cdot \tilde{\mathbf{S}}_{Wj}(\mathbf{k}) \cdot T_{CS}(\mathbf{k}, l'm'), \quad (5.7)$$

where the component matrices are given by

$$T_{CS}(\mathbf{k}, lm) = \begin{bmatrix} \mathbf{T}_{CS}^{+-}(\mathbf{k}, lm) \\ \mathbf{T}_{CS}^{-+}(\mathbf{k}, lm) \end{bmatrix}, \quad (5.8a)$$

$$T_{SC}(lm, \mathbf{k}) = [\mathbf{T}_{SC}^{+-}(lm, \mathbf{k}) \quad \mathbf{T}_{SC}^{++}(lm, \mathbf{k})], \quad (5.8b)$$

$$\tilde{\mathbf{S}}_{Wj}(\mathbf{k}) = \begin{bmatrix} \tilde{\mathbf{S}}_C^{++}(Z_{Lj}\mathbf{k}) & 0 \\ 0 & \tilde{\mathbf{S}}_C^{--}(Z_{Uj}\mathbf{k}) \end{bmatrix}, \quad (5.9a)$$

$$\tilde{\mathbf{S}}_{iW}(\mathbf{k}) = \begin{bmatrix} \tilde{\mathbf{S}}_C^{--}(Z_{iL}\mathbf{k}) & 0 \\ 0 & \tilde{\mathbf{S}}_C^{++}(Z_{iU}\mathbf{k}) \end{bmatrix}, \quad (5.9b)$$

and

$$\tilde{\mathbf{Z}}_{TW}(\mathbf{k}) = \begin{bmatrix} \mathbf{Z}_w^{-1} & \tilde{\mathbf{S}}_C^{++}(Z_{LU}\mathbf{k}) \\ \tilde{\mathbf{S}}_C^{--}(Z_{UL}\mathbf{k}) & \mathbf{Z}_w^{-1} \end{bmatrix}^{-1}. \quad (5.10)$$

The physical interpretation of equation (5.7) is similar to the interpretation of relation (5.2), except that two separate sets of expansion coefficients are now used for the flow field incoming to the lower and upper walls, which is reflected in the corresponding block structure of matrices (5.8)–(5.10). The matrix $T_{\text{CS}}(\mathbf{k}, l'm')$ transforms the field produced by a force multipole at the position \mathbf{R}_j into the Cartesian basis; the basis fields $\mathbf{v}_{\mathbf{k}\sigma}^+$ are used in the region $Z < z_j$ and the basis fields $\mathbf{v}_{\mathbf{k}\sigma}^-$ in the region $Z > z_j$, consistent with relation (4.4). The Cartesian fields are then translated to the positions of the respective walls by the matrix $\tilde{\mathbf{S}}_{\text{W}j}(\mathbf{k})$. The matrix $\tilde{\mathbf{Z}}_{\text{TW}}(\mathbf{k})$, defined by equation (5.10), describes the interaction of the flow field with both walls. We note that this matrix involves the displacements matrices $\tilde{\mathbf{S}}_{\text{C}}^-(Z_{\text{UL}}\mathbf{k})$ and $\tilde{\mathbf{S}}_{\text{C}}^+(Z_{\text{LU}}\mathbf{k})$, which correspond to the propagation of the flow field between the walls in the multiple-reflection process. After reflection from the walls is completed, the matrix $\tilde{\mathbf{S}}_{i\text{W}}(\mathbf{k})$ propagates the flow field to the target point i , and the matrix $T_{\text{SC}}(lm, \mathbf{k})$ transforms it back into the spherical representation.

Due to the symmetries of the 3×3 transformation and displacement matrices, the corresponding symmetry relations

$$T_{\text{CS}}(\mathbf{k}, lm) = [T_{\text{SC}}(lm, \mathbf{k})]^\dagger, \quad (5.11a)$$

$$\tilde{\mathbf{S}}_{\text{W}i}(\mathbf{k}) = [\tilde{\mathbf{S}}_{i\text{W}}(\mathbf{k})]^\dagger, \quad (5.11b)$$

$$\tilde{\mathbf{Z}}_{\text{TW}}(\mathbf{k}) = [\tilde{\mathbf{Z}}_{\text{TW}}(\mathbf{k})]^\dagger \quad (5.11c)$$

are satisfied by the matrices (5.8)–(5.10). Equation (5.7) thus implies that the Green matrix (5.6) satisfies the Lorentz symmetry (5.3).

6. Numerical implementation

The evaluation of the resistance matrix ζ_{ij}^{AB} from relations given in Appendix B requires solving the linear algebraic equation (3.8) for the array of induced-force multipolar moments in order to obtain the generalized friction coefficients $F_{ij}(lm\sigma | l'm'\sigma')$. In expression (3.9) for the matrix \mathbf{M}_{ij} the single particle scattering matrix \mathbf{Z}_i and the unbounded-space Green's matrix \mathbf{G}_{ij}^0 are known explicitly (Felderhof & Jones 1989; Cichocki *et al.* 1988). The remaining term—the two-wall contribution \mathbf{G}'_{ij} —is evaluated numerically, using relations (5.6)–(5.10) along with our expressions for the Cartesian displacement matrices (4.12), the transformation matrices (4.8), and the single-wall scattering matrix (4.19).

Taking into account the structure (4.6) of the transformation matrices $\mathbf{T}_{\text{SC}}^{+\mp}$ and $\mathbf{T}_{\text{CS}}^{\pm-}$, the angular integral in equation (5.1) can be performed analytically. The integration yields the result in the form of a Hankel transform of the order $m' - m$. Accordingly, only a one-dimensional integral in equation (5.6) has to be performed numerically. The numerical integration is straightforward when the lateral separation between particles i and j is small compared to the wall separation. For large interparticle separations ρ_{ij} , however, the integration is more difficult due to the oscillatory behavior of the integrand.

To avoid numerical integration of a highly oscillatory function, the Fourier amplitude in (5.6) is decomposed

$$\tilde{\Psi}(\mathbf{k}) = \tilde{\Psi}_{\text{L}}(\mathbf{k}) + \tilde{\Psi}_{\text{U}}(\mathbf{k}) + \delta\tilde{\Psi}(\mathbf{k}) \quad (6.1)$$

into the superposition of the single-wall contributions $\tilde{\Psi}_{\text{L}}$ and $\tilde{\Psi}_{\text{U}}$, and the remaining part $\delta\tilde{\Psi}$ representing hydrodynamic interactions between the walls. From an analysis of

expression (5.2) we find that the magnitude of the single-wall Fourier amplitudes $\tilde{\Psi}_L(\mathbf{k})$ and $\tilde{\Psi}_U(\mathbf{k})$ for large k is

$$\tilde{\Psi}_\alpha(\mathbf{k}) \sim e^{-k\Delta_{ij}^{(\alpha)}}, \quad \alpha = L, U, \quad (6.2)$$

where $\Delta_{ij}^{(\alpha)}$ is the vertical offset between the point i and the reflection of point j in the wall α . In contrast, the large- k behavior of the wall-interaction part of Fourier amplitude (6.1) is

$$\delta\tilde{\Psi}(\mathbf{k}) \sim e^{-k\tilde{\Delta}_{ij}}, \quad (6.3)$$

where

$$\tilde{\Delta}_{ij} = 2H - |Z_{ij}| > H. \quad (6.4)$$

The lengthscale $\tilde{\Delta}_{ij}$ equals the vertical offset $|Z_i - Z_j''|$ between the target point i and the closer of the two second-order images of the source point j . Since $\delta\tilde{\Psi}(\mathbf{k})$ decays on the wave-vector scale set by the distance between the walls $H > \min(\Delta_{ij}^{(L)}, \Delta_{ij}^{(U)})$, a smaller number of oscillations of the Fourier modes contributes to the integral after the single-wall terms have been subtracted.

In our algorithm, the short-range function $\delta\tilde{\Psi}(\mathbf{k})$ is integrated numerically. The one-particle contributions $\tilde{\Psi}_L(\mathbf{k})$ and $\tilde{\Psi}_U(\mathbf{k})$ are evaluated analytically, using the explicit image-representation expressions derived in Cichocki & Jones (1998). In this way we avoid integrating a highly oscillatory function when the particles are close to a wall. The procedure can be further improved, either by subtracting several terms associated with higher-order wall reflections of the source multipole (Bhattacharya & Bławdziewicz 2002a), or by using asymptotic formulas for the integrals (5.6). We have recently derived a complete set of such expressions, which will be presented in a separate publication.

In order to improve convergence with the order l_{\max} of the multipoles included in the calculation we employ a standard technique, originally introduced by Durlofsky *et al.* (1987). Accordingly, the lubrication forces that cause a slow convergence of the results with l_{\max} are included in the friction matrix using a superposition approximation. Both, the interparticle and particle-wall lubrication corrections are included in this way. Following the implementation of this method by Cichocki *et al.* (2000) for a single wall problem, we represent the elements of resistance matrix ζ_{ij} in the form

$$\zeta_{ij} = \zeta_{ij}^{\text{sup},2} + \zeta_{ij}^{\text{sup},w} + \Delta\zeta_{ij}. \quad (6.5)$$

Here $\zeta_{ij}^{\text{sup},2}$ denotes the superposition of two-particle resistance matrices evaluated for isolated particle pairs in the unbounded space, and

$$\zeta_{ij}^{\text{sup},w} = \delta_{ij} \sum_{\alpha=L,U} \zeta_i^\alpha(i). \quad (6.6)$$

is the superposition of one-particle contributions in the presence of individual walls. The one-particle contributions can be evaluated using a series expansion of resistance coefficients in inverse powers of particle-wall separation (Cichocki & Jones 1998) in combination with the appropriate lubrication results (Kim & Karrila 1991). The two-particle superposition contributions $\zeta_{ij}^{\text{sup},w}$ are evaluated in a similar way. The convergence with the multipolar truncation order l_{\max} for the quantity $\Delta\zeta_{ij}$ is fast; some convergence tests are presented in Ref. I.

In the present implementation of our method, the numerical cost scales as $O(N^3)$ with the number of particles N , because the linear equation (3.9) is solved by inversion of the matrix \mathbf{M} . However, the numerical efficiency of our algorithm can be substantially

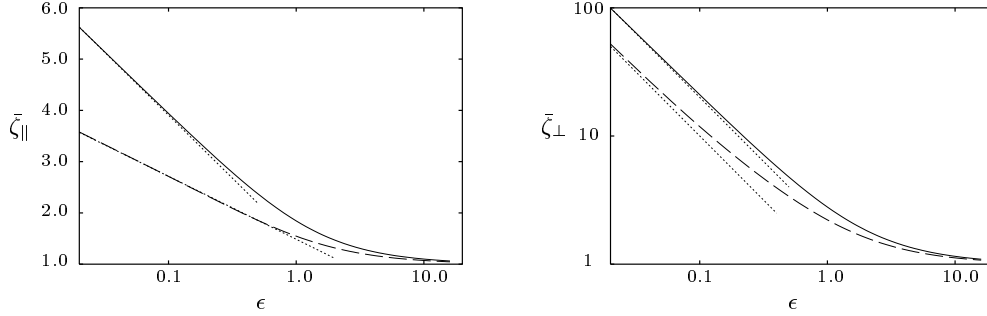


FIGURE 1. Lateral and vertical components of the translational friction matrix (7.3) for a single sphere between two parallel walls, versus dimensionless gap (7.4). Center particle position $h = \frac{1}{2}H$ (solid line); off-center position $h = \frac{1}{3}H$ (dashed line). Dotted lines represent the lubrication results (7.5).

improved by applying fast-multipole or PPPM acceleration methods in combination with asymptotic expressions for the elements of the matrix \mathbf{M} .

7. Results

In this section we present a set of numerical results for hydrodynamic interactions in systems of spherical particles confined between two parallel planar walls. Our goal is both, to illustrate typical behavior of the hydrodynamic friction matrix for particles in the confined region, and to demonstrate the capabilities of our numerical algorithm. The results for a single particle and for pairs of particles, shown in figures 1–8, were obtained using the multipolar approximation with the truncation at the order $l_{\max} = 12$. This truncation is sufficient to obtain results with the accuracy better than the resolution of the plots, even for the smallest wall separation H considered. The multi-particle results in figures 9–11 were obtained using $l_{\max} = 8$.

7.1. Single particle

In figure 1, the lateral and vertical friction coefficients

$$\zeta_{\parallel} = \zeta_{11}^{tt\,xx} = \zeta_{11}^{tt\,yy}, \quad \zeta_{\perp} = \zeta_{11}^{tt\,zz} \quad (7.1)$$

are shown for a single particle at the center and off-center positions

$$h = \frac{1}{2}H, \quad h = \frac{1}{3}H, \quad (7.2a, b)$$

where h is the distance of the particle from the lower wall. The results are normalized by the Stokes friction coefficient $\zeta_0 = 6\pi\eta a$,

$$\bar{\zeta}_{\parallel} = \zeta_{\parallel}/\zeta_0, \quad \bar{\zeta}_{\perp} = \zeta_{\perp}/\zeta_0, \quad (7.3)$$

and are plotted versus the normalized gap

$$\epsilon = h/a - 1 \quad (7.4)$$

between the particle and the lower wall. As expected, for small values of the gap, the lateral and vertical resistance coefficients approach the asymptotic lubrication behavior (in figure 1 indicated by dotted lines). For $h = \frac{1}{2}H$ the lubrication behavior is

$$\bar{\zeta}_{\parallel} = -\frac{16}{15} \log \epsilon + C\left(\frac{1}{2}\right), \quad \bar{\zeta}_{\perp} = 2\epsilon^{-1}, \quad (7.5a)$$

where the singular terms correspond to the superposition of two particle–wall lubrication regions (cf. lubrication expressions given by Cichocki & Jones 1998). For the off-center position $h = \frac{1}{3}H$ there is only one lubrication region, thus

$$\bar{\zeta}_{\parallel} = -\frac{8}{15} \log \epsilon + C(\frac{1}{3}), \quad \bar{\zeta}_{\perp} = \epsilon^{-1}. \quad (7.5b)$$

A comparison of the numerical results shown in figure 1 with the asymptotic behavior (7.5) yields $C(\frac{1}{2}) = 1.45$ and $C(\frac{1}{3}) = 1.49$.

We note that our one-particle results agree with the numerical calculation by Ganatos *et al.* (1980*b,a*) and with our earlier results (Bhattacharya & Bławdziewicz 2002*b*) obtained by an image-representation method (Bhattacharya & Bławdziewicz 2002*a*).

7.2. Two particles

Sample results for the translational components of the two-particle resistance matrix

$$\bar{\zeta}_{ij}^{\alpha\beta} = \zeta_{ij}^{\text{tt}\alpha\beta} / \zeta_0, \quad i, j = 1, 2, \quad (7.6)$$

(where $\alpha, \beta = x, y, z$) are presented in figures 2–8. The results in figures 2–4 are shown for horizontal particle configurations $h_1 = h_2 = h$, where h_i is the distance of particle i from the lower wall. As for a single sphere, we consider the center and off-center positions (7.2). The relative horizontal displacement of the particles is

$$\boldsymbol{\rho}_{12} = \rho_{12} \hat{\mathbf{e}}_x. \quad (7.7)$$

To emphasize the crossover between the three-dimensional behavior for $\rho_{12} \ll H$ and a quasi-two-dimensional behavior for $\rho_{12} \gg H$, we discuss our results in terms of the dimensionless variables scaled by the distance between the walls H ,

$$\tilde{\rho} = \rho_{12}/H, \quad \tilde{a} = a/H, \quad \tilde{L} = \tilde{\rho} - 2\tilde{a}. \quad (7.8a, b, c)$$

The resistance coefficients in figures 2–4 are plotted versus the dimensionless separation between the particle surfaces \tilde{L} .

Self-resistance coefficients

Figures 2 and 3 illustrate the behavior of the diagonal components of the translational self- and mutual resistance matrices $\bar{\zeta}_{11}^{\alpha\alpha}$ and $\bar{\zeta}_{12}^{\alpha\alpha}$, respectively, and figure 4 shows the off-diagonal elements $\bar{\zeta}_{11}^{xz}$ and $\bar{\zeta}_{12}^{xz}$. The remaining coefficients of the two-particle translational resistance matrix either vanish or can be related to the above coefficients by symmetry.

The results for the resistance coefficients $\bar{\zeta}_{11}^{\alpha\alpha}$ presented in figure 2 are scaled by the corresponding single-particle friction coefficients (7.3). For small distances between the particle surfaces $\tilde{L} \ll \tilde{a}$ the longitudinal resistance coefficient $\bar{\zeta}_{11}^{xx}$ is dominated by the $O(\tilde{L}^{-1})$ interparticle lubrication friction; the lubrication behavior of the components transverse to the direction of the line connecting the particle centers is $\bar{\zeta}_{11}^{yy}, \bar{\zeta}_{11}^{zz} \sim \log \tilde{L}$.

In the intermediate regime $\tilde{\rho} \approx 1$ the two-particle friction matrix undergoes a crossover to a quasi-two-dimensional far-field asymptotic behavior at large interparticle distances. A signature of the crossover is the kink seen in the plot of $\bar{\zeta}_{11}^{yy}$ for the particles at the center position $h = \frac{1}{2}H$. For large interparticle separations $\tilde{\rho} \gg 1$, the lateral components of the self-friction matrix approach the one-particle asymptotic value as

$$\bar{\zeta}_{11}^{xx} \approx \bar{\zeta}_{11}^{yy} = \bar{\zeta}_{\parallel} + O(\tilde{\rho}^{-4}), \quad \tilde{\rho} \gg 1. \quad (7.9)$$

This result stems from the far-field behavior of the disturbance velocity produced by the particles. For the lateral motion the far-field disturbance decays as $O(\tilde{\rho}^{-2})$, as shown in Ref. I. Since the contribution of the second particle to the self-components of the friction matrix $\bar{\zeta}_{11}^{\alpha\alpha}$ involves the field scattered back to the first particle, the asymptotic behavior

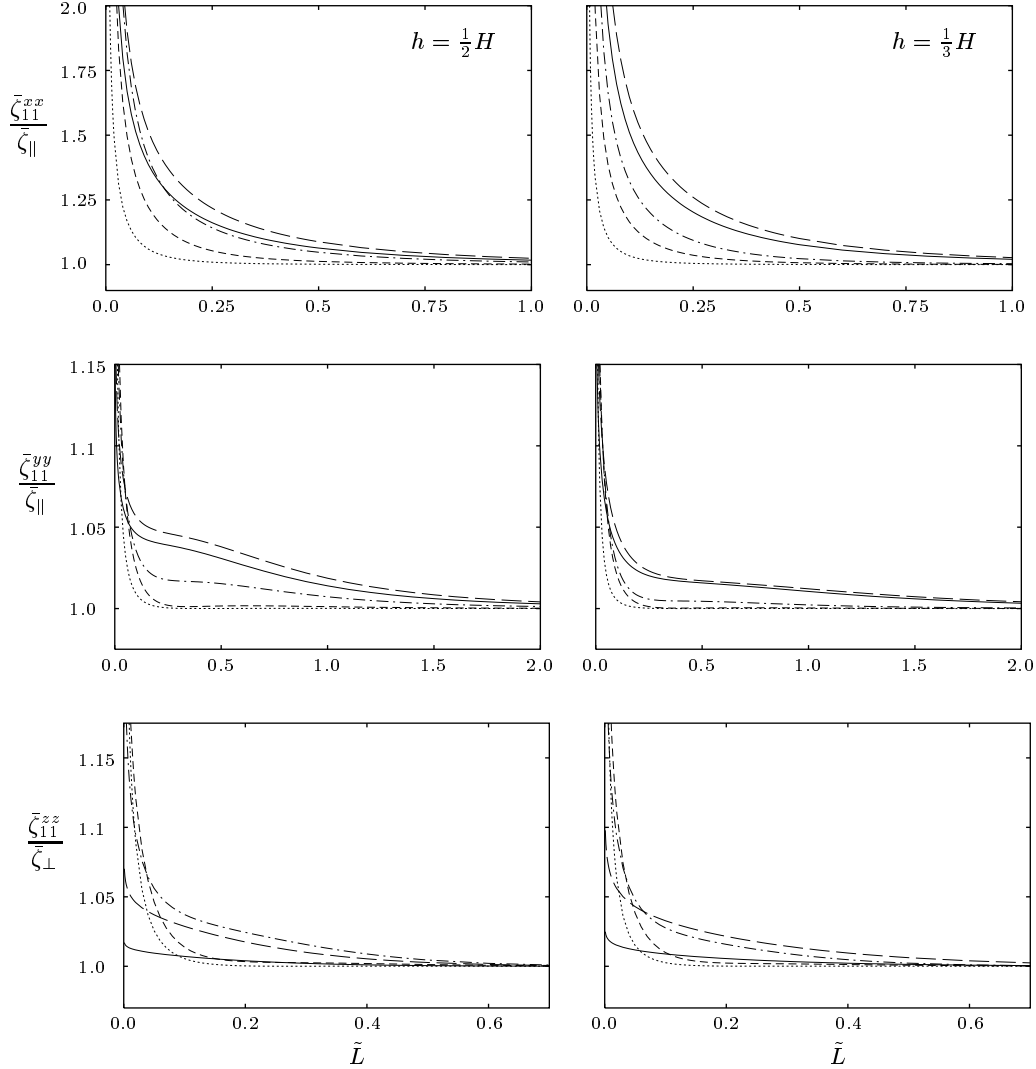


FIGURE 2. Diagonal components of translational self-resistance matrix (7.6) for pair particles between two planar walls, scaled by corresponding one-particle values, versus dimensionless distance (7.8c) between particle surfaces. Walls are in planes $z = 0, H$, and particles are on axis x . The left and right panels correspond to center and off-center particle configurations (as indicated). Dimensionless gap between the particles and the closer wall $\epsilon = 0.02$ (solid line); $\epsilon = 0.1$ (long-dashed); $\epsilon = 1.0$ (dash-dotted); $\epsilon = 4$ (short-dashed); $\epsilon = 16$ (dotted).

(7.9) is obtained. In contrast, the disturbance field corresponding to the vertical motion decays exponentially, which yields an exponential approach of the vertical component of the friction matrix $\bar{\zeta}_{11}^{zz}$ to the one-particle value $\bar{\zeta}_{\perp}$.

Mutual resistance coefficients

An analogous reasoning applied to the mutual components of the friction matrix yields the asymptotic behavior

$$\bar{\zeta}_{12}^{yy} \approx -\bar{\zeta}_{12}^{xx} = A\tilde{\rho}^{-2} + O(\tilde{\rho}^{-4}), \quad \tilde{\rho} \gg 1, \quad (7.10)$$

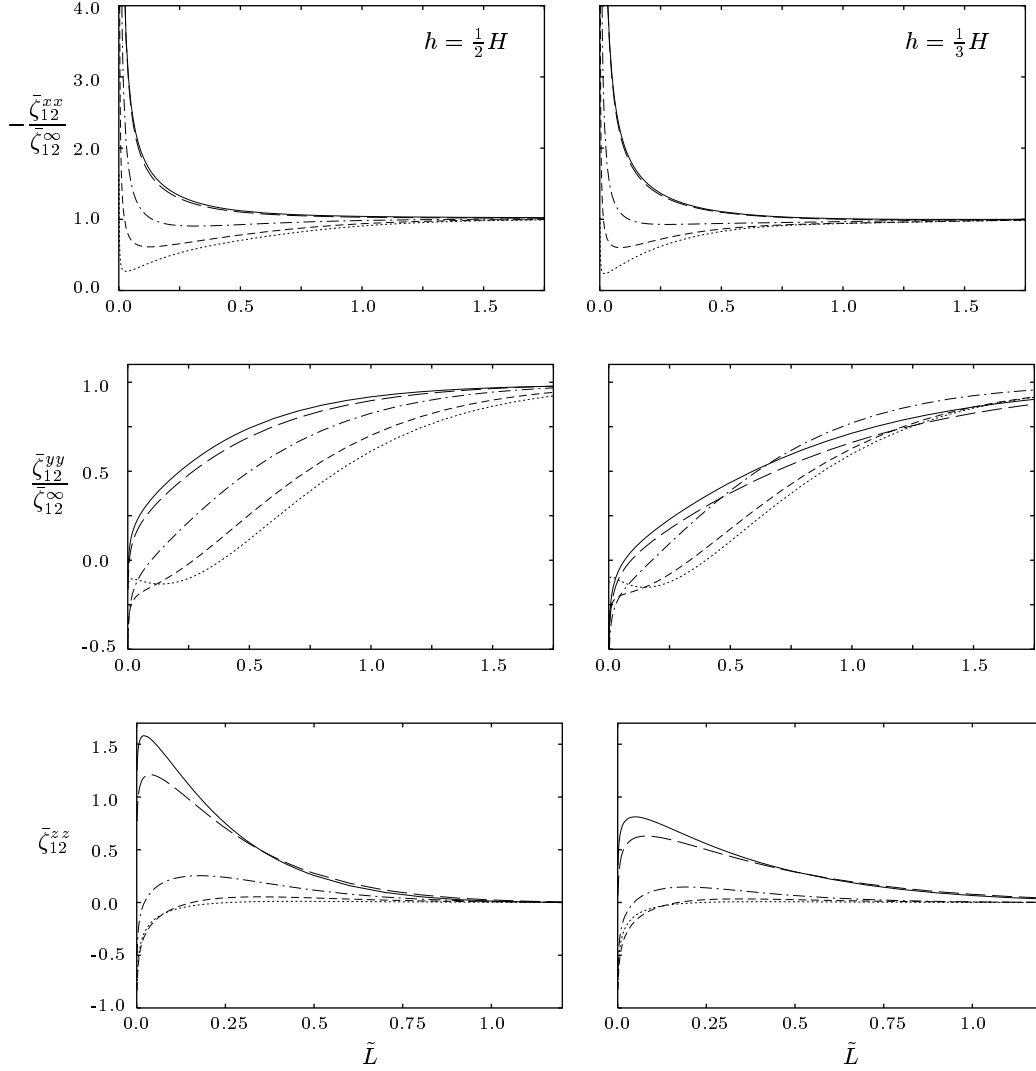


FIGURE 3. Same as figure 2, except that for mutual components of the resistance matrix. The lateral components $\bar{\zeta}_{12}^{xx}$ and $\bar{\zeta}_{12}^{yy}$ are scaled by the asymptotic result $\bar{\zeta}_{12}^{\infty} = A\tilde{\rho}^{-2}$ corresponding to relation (7.10), and the vertical component is $\bar{\zeta}_{12}^{zz}$ unscaled.

where the amplitude $A > 0$ depends on the size of the particles and on their vertical positions in the gap. Note that the sign of the transverse resistance coefficient $\bar{\zeta}_{12}^{yy}$ at large interparticle distances is opposite to the sign of the corresponding coefficient in the unbounded space.

The results for $\bar{\zeta}_{12}^{xx}$ and $\bar{\zeta}_{12}^{yy}$ shown in figure 3 are scaled using expression (7.10), with the amplitude A plotted in figure 5 (discussed below). Since $\bar{\zeta}_{12}^{zz}$ decays exponentially for large $\tilde{\rho}$, the results for this component are presented unscaled. Similar to the results in figure 2 for the self-resistance matrix, the diagonal components of the mutual resistance matrix have a lubrication singularity for particles in contact, and for $\tilde{\rho} = O(1)$ they exhibit a crossover to the asymptotic $O(\tilde{\rho}^{-2})$ far-field behavior in the regime $\tilde{\rho} \gg 1$. The

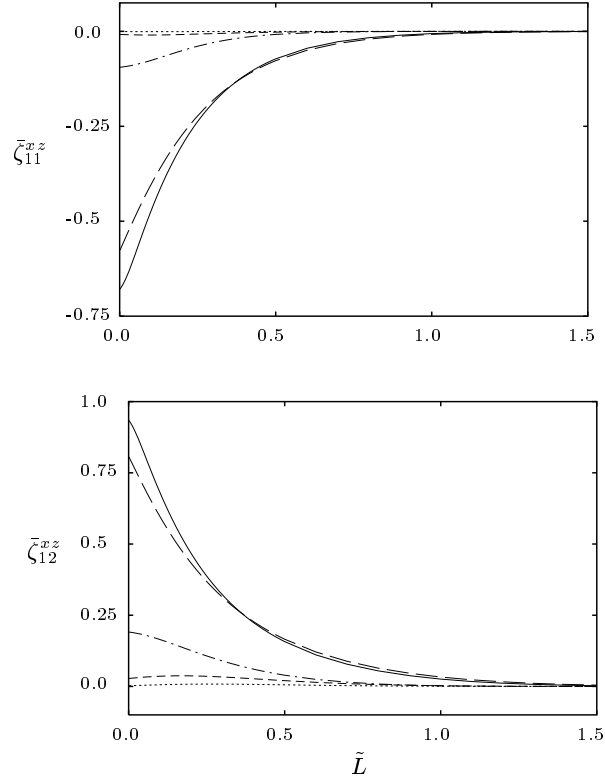


FIGURE 4. Cross components of self- and mutual resistance matrix (7.6) for the off-center particle configuration $h = \frac{1}{3}H$. Dimensionless particle-wall gaps ϵ corresponding to different lines are the same as in figure 2.

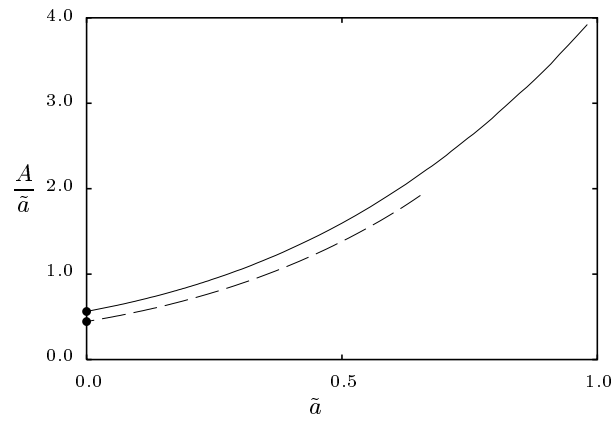


FIGURE 5. Amplitude A of the $O(\tilde{\rho}^{-2})$ far field asymptotic behavior (7.10) of the mutual resistance matrix, versus particle size normalized by distance between walls $\tilde{a} = a/H$. Center particle configuration $h_1 = h_2 = \frac{1}{2}H$ (solid line); off center configuration $h_1 = h_2 = \frac{1}{3}H$ (dashed line). Circles represent the corresponding asymptotic values (7.11).

$\rho/2a$	$\bar{\zeta}_{11}^{c,xx}$	$\bar{\zeta}_{11}^{c,yy}$	$\bar{\zeta}_{11}^{c,zz}$	$\bar{\zeta}_{12}^{c,xx}$	$\bar{\zeta}_{12}^{c,yy}$	$\bar{\zeta}_{12}^{c,zz}$
1.01	15.08	2.31	3.26	-13.75	-0.51	-0.24
1.1	3.35	1.98	2.95	-1.99	-0.117	0.132
2.0	1.93	1.87	2.80	-0.368	0.200	0.117
5.0	1.85	1.85	2.79	-0.064	0.063	0.00015

TABLE 1. Normalization factors (7.13) for the configurations represented in figures 6 and 7.

near-field and far-field region are most pronounced for large values of the particle-wall gap ϵ (i.e., for $\tilde{a} \ll 1$) because of the lengthscale separation.

Cross-terms

The cross-elements of the self- and mutual friction matrix $\bar{\zeta}_{11}^{xz}$ and $\bar{\zeta}_{12}^{xz}$ are shown (unscaled) in figure 4. Since for the center particle position (7.2a) these components vanish by symmetry, the results are presented only for the off-center configuration (7.2b). The nonzero values of the cross-resistance coefficients $\bar{\zeta}_{11}^{xz}$ and $\bar{\zeta}_{12}^{xz}$ arise indirectly, due to the asymmetry of the flow field scattered from the walls. Therefore, for $\tilde{L} = 0$ there is no lubrication singularity. The cross-resistance coefficients involve vertical particle motion; thus, for large interparticle separations $\bar{\zeta}_{11}^{xz}$ and $\bar{\zeta}_{12}^{xz}$ decay exponentially.

Amplitude of the far-field asymptotic behavior

The behavior (7.9) and (7.10) of the two-particle resistance coefficients for $\tilde{\rho} \gg 1$ is consistent with the asymptotic expressions derived by Liron & Mochon (1976) for the far-field flow produced by Stokeslets oriented in the direction parallel and normal to the walls. Using the Liron–Mochon expression and applying the Stokes resistance formula to evaluate forces acting on small particles in the space between the walls yields the asymptotic behavior (7.10), with the amplitude given by

$$\frac{A}{\tilde{a}} = 9\tilde{h}_1(1 - \tilde{h}_1)\tilde{h}_2(1 - \tilde{h}_2) + O(\tilde{a}), \quad (7.11)$$

where $\tilde{h}_i = h_i/H$. Figure 5 shows the dependence of the far-field amplitude A on the dimensionless particle size \tilde{a} ; the limiting result (7.11) is indicated by circles.

We emphasize that the far-field form of the disturbance flow produced by particles in a domain bounded by parallel walls, and the corresponding properties of the resistance matrix are important for understanding the macroscopic dynamics of suspensions in slit-pore geometries. A more detailed analysis of this problem will be given elsewhere.

Skew configurations

So far we have focused on horizontal particle configurations with both particles at the same distance from the walls. In figures 6–8 we consider skew configurations with the vertical positions

$$h_1 = h, \quad h_2 = H - h. \quad (7.12)$$

Figures 6 and 7 show the diagonal components $\bar{\zeta}_{11}^{\alpha\alpha}$ and $\bar{\zeta}_{12}^{\alpha\alpha}$ of the self- and mutual resistance matrices, and figure 8 presents the off-diagonal components $\bar{\zeta}_{11}^{xz}$ and $\bar{\zeta}_{12}^{xz}$. The results are plotted versus the normalized particle-wall gap (7.4).

The diagonal resistance coefficients $\bar{\zeta}_{ij}^{\alpha\alpha}$ in figures 6 and 7 are scaled by the value

$$\bar{\zeta}_{ij}^{c,\alpha\alpha} = \bar{\zeta}_{ij}^{\alpha\alpha} (h = \frac{1}{2}H), \quad (7.13)$$

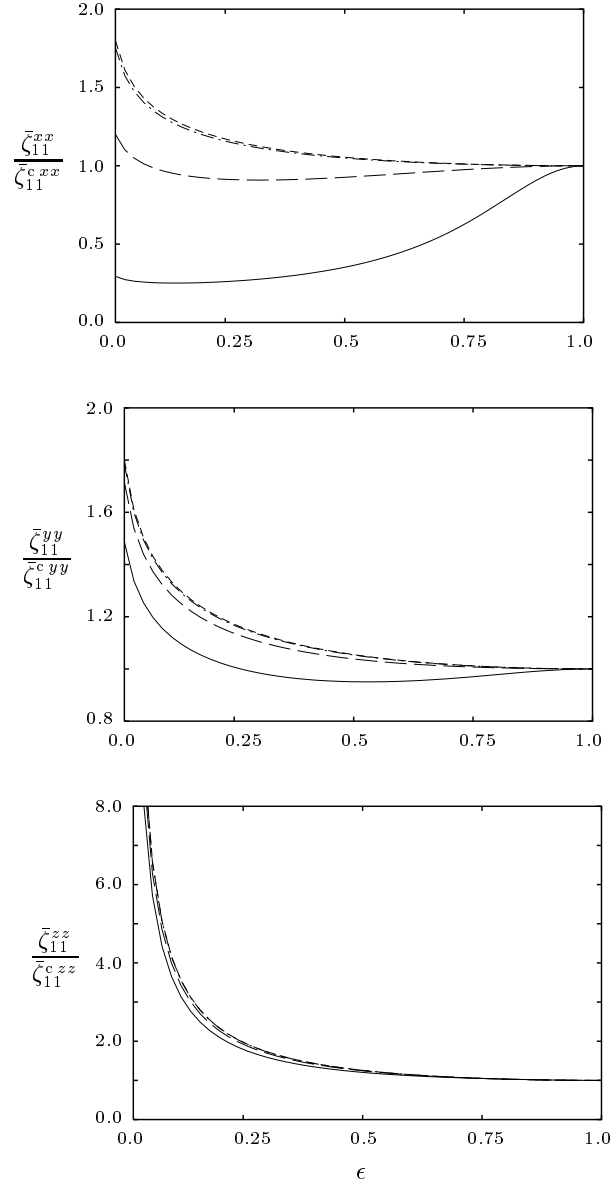


FIGURE 6. Diagonal components of translational self-resistance matrix for skew configurations (7.12) of a particle pair between two walls separated by distance $H/2a = 2$, versus normalized particle-wall gap (7.4). The results are scaled by the value (7.13) for the center position, which corresponds to $\epsilon = 1$. Lateral particle separation $\rho/2a = 1.01$ (solid lines); 1.1 (dashed); 2 (dash-dotted); 5 (dotted).

corresponding to the center configuration of the particle pair at a given lateral separation ρ and wall-to-wall distance H . The resistance coefficients for the center configuration (7.13) have been discussed above; the values of the normalization factors for the parameter values represented in figures 6 and 7 are listed in table 1.

For large lateral interparticle distances, the self-resistance coefficients, shown in figure 6, approach the corresponding one-particle results. We note that due to the fast asymp-

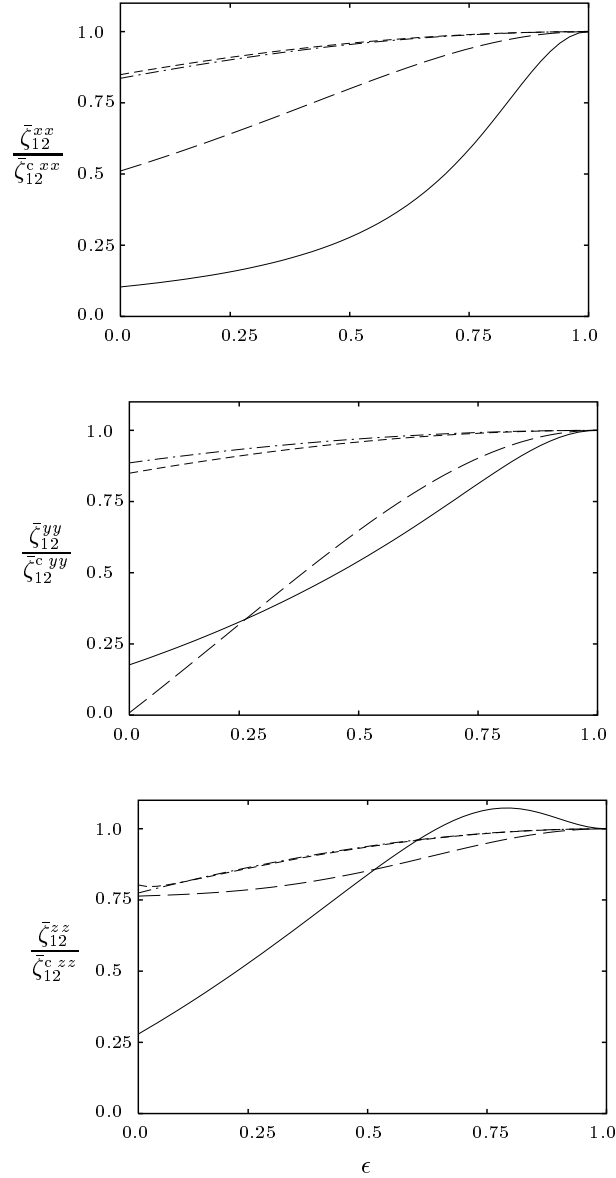


FIGURE 7. Same as figure 6, except that for mutual friction coefficients.

otic approach (7.9), the results for $\rho/2a = 5$ essentially coincide with the one-particle values. For small particle–wall gaps, the lateral coefficients $\bar{\zeta}_{11}^{xx}$ and $\bar{\zeta}_{11}^{yy}$ exhibit the logarithmic lubrication singularity, and the vertical component $\bar{\zeta}_{11}^{zz}$ has the $1/\epsilon$ singularity. The rapid variation of the longitudinal coefficient $\bar{\zeta}_{11}^{xx}$ in the regime $\epsilon \approx 1$ (center particle positions) for $\rho/2a = 1.01$ results from the strong lubrication interaction between the particles. The same remark applies to the mutual longitudinal coefficient $\bar{\zeta}_{12}^{xx}$ shown in figure 7.

According to the results in table 1, the mutual resistance coefficients approach zero for large interparticle distances. The far-field behavior is consistent with the asymptotic

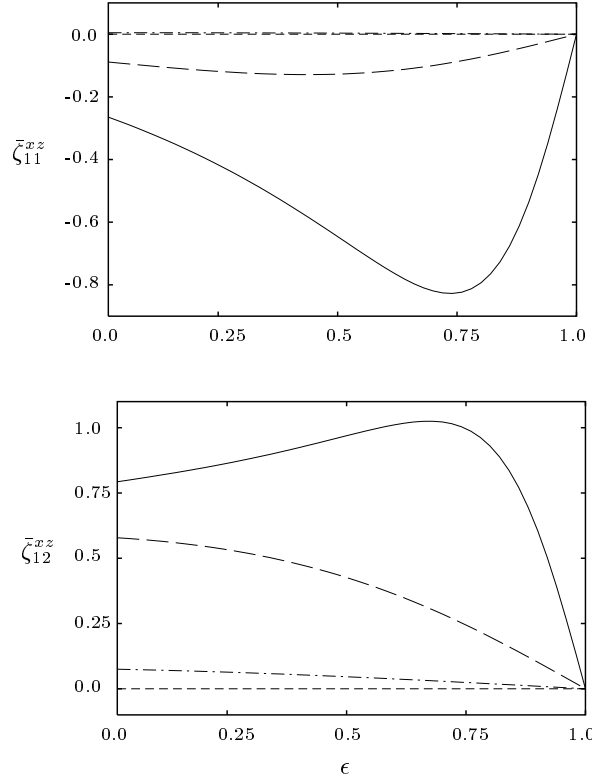


FIGURE 8. Same as figure 6, except that for self- and mutual cross friction coefficients, and that the results are unscaled.

expression (7.10) for the lateral components $\bar{\zeta}_{12}^{xx}$ and $\bar{\zeta}_{12}^{yy}$ and the asymptotic exponential decay for the vertical component $\bar{\zeta}_{11}^{zz}$. We note that for small and moderate interparticle distances there is no simple relation between the components $\bar{\zeta}_{12}^{xx}$ and $\bar{\zeta}_{12}^{yy}$; however $\bar{\zeta}_{12}^{yy} \approx -\bar{\zeta}_{12}^{xx}$ for $\tilde{\rho} \gg 1$, in agreement with equation (7.10).

The off-diagonal components $\bar{\zeta}_{11}^{xz}$ and $\bar{\zeta}_{12}^{xz}$, shown unscaled in figure 8, are exponentially small for $\tilde{\rho} \gg 1$. For both particles at the center of the space between the walls these components vanish by symmetry.

7.3. Multi-particle systems

In figures 9–11 we present some results for hydrodynamic resistance functions of rigid linear arrays of N touching spheres. The spheres are positioned on a line parallel to the axis x at the center of the space between the walls, i.e.,

$$h_i = \frac{1}{2}H, \quad i = 1, \dots, N. \quad (7.14)$$

The diagonal components of the translational resistance matrix of the array treated as a single rigid body, evaluated per one sphere,

$$\bar{\zeta}_C^{\alpha\alpha} = (N\zeta_0)^{-1} \sum_{i,j=1}^N \zeta_{ij}^{\text{tt}\alpha\alpha}, \quad \alpha = x, y, z, \quad (7.15)$$

are plotted in figure 9 versus the number of spheres N in the chain. The results for the

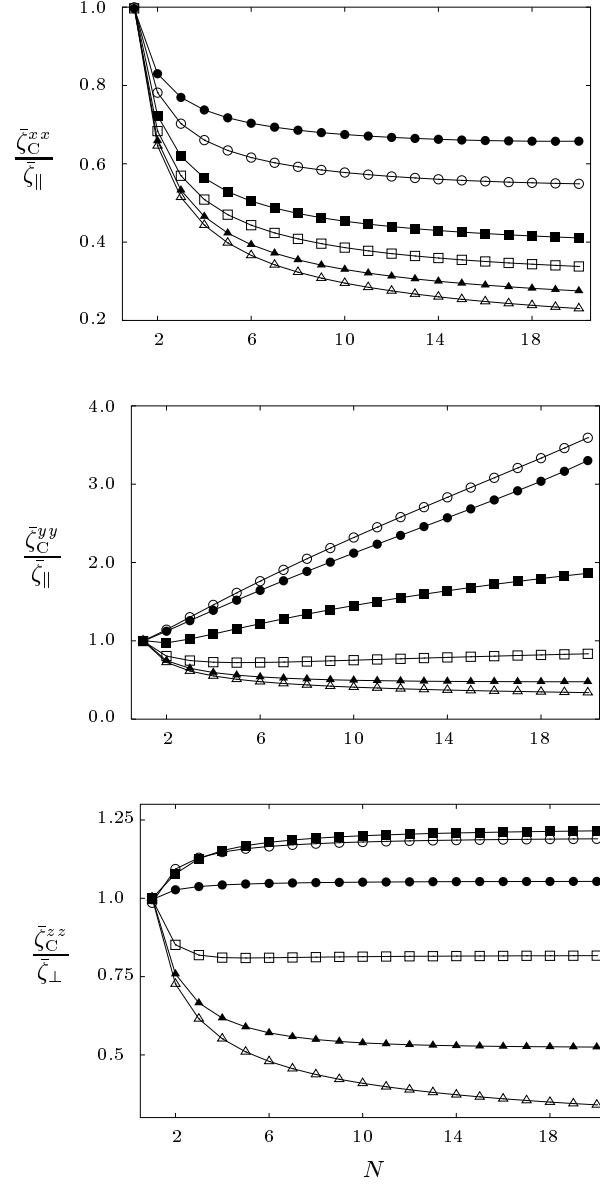


FIGURE 9. Resistance coefficients per particle (7.15) of rigid linear arrays of touching spheres on a line parallel to axis x at the center position (7.14), scaled by corresponding one-particle values (7.3), versus number of spheres N . Dimensionless gap between the particles and walls $\epsilon = 0.02$ (solid circles); $\epsilon = 0.1$ (open circles); $\epsilon = 1.0$ (solid squares); $\epsilon = 4$ (open squares); $\epsilon = 16$ (solid triangles); $\epsilon = \infty$ (open triangles).

longitudinal and transverse components $\bar{\zeta}_C^{xx}$ and $\bar{\zeta}_C^{yy}$ are shown normalized by the lateral one-particle resistance coefficient $\bar{\zeta}_\parallel$; the vertical component $\bar{\zeta}_C^{zz}$ is normalized by $\bar{\zeta}_\perp$. The results indicate that for large separations between the walls, when compared to the chain length, all three components of the resistance matrix $\bar{\zeta}_C^{\alpha\alpha}$ decrease monotonically with N , and behave as $1/\log N$ for $1 \ll N \ll H/2a$. We also find that $\bar{\zeta}_C^{yy} \simeq \bar{\zeta}_C^{zz} \simeq 2\bar{\zeta}_C^{xx}$ in this regime (Bławdziewicz *et al.* 2005).

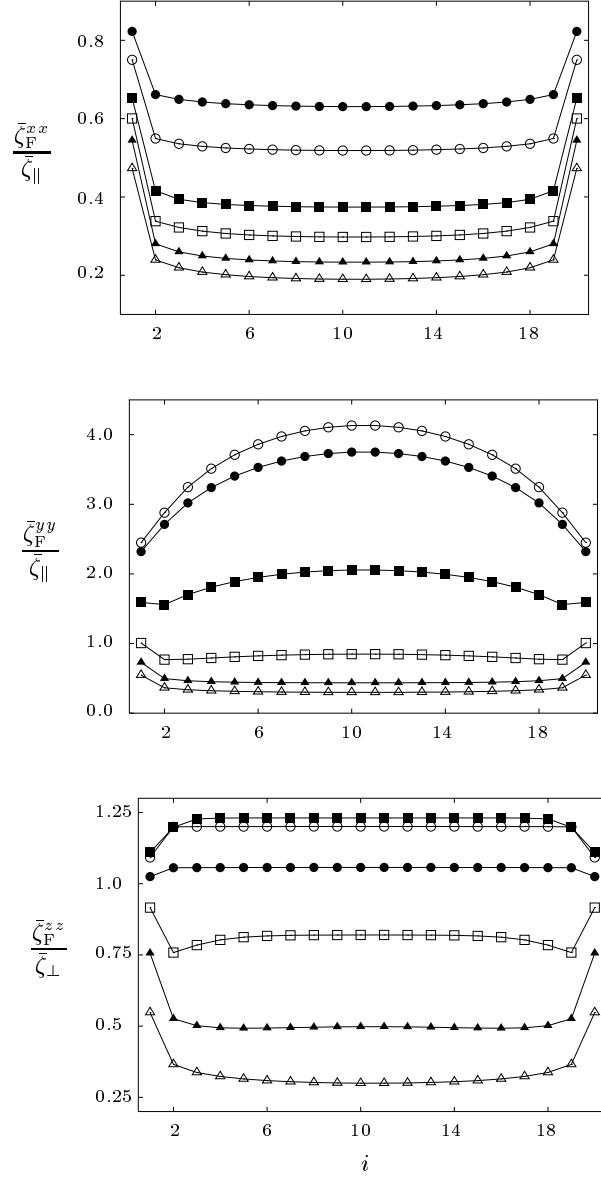


FIGURE 10. Resistance coefficients (7.16a) representing the total forces (7.17a) on individual spheres in the chain of length $N = 20$, scaled by corresponding one-particle values (7.3), versus particle number in the chain. The configuration of the chain and the dimensionless particle-wall gaps ϵ are the same as in figure 9.

For moderate and small values of the wall-to-wall distance H , however, the behavior of each component $\bar{\zeta}_C^{\alpha\alpha}$ of the chain resistance matrix is qualitatively different. The longitudinal component $\bar{\zeta}_C^{xx}$ decreases monotonically with N , which is similar to the behavior in the unbounded space, but the variation is smaller. The vertical component $\bar{\zeta}_C^{zz}$ initially increases with N , and then saturates at a constant value that depends on the wall separation H . In contrast, for small H , the transverse component $\bar{\zeta}_C^{yy}$ increases linearly with

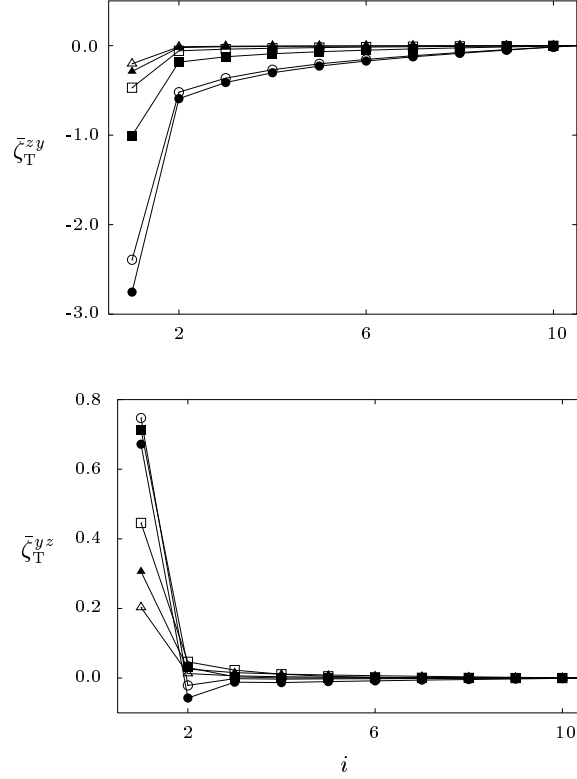


FIGURE 11. Same as figure 10, except that for resistance coefficients (7.16b) representing the total torques (7.17b) on individual spheres, and that the results are plotted unscaled. Only half of the chain is shown; the resistance coefficients are antisymmetric with respect to the chain center.

N in the range of chain lengths shown. Additional numerical simulations for chains with the length up to $N=100$ (not presented) indicate that the resistance coefficients $\bar{\zeta}_C^{yy}$ eventually saturate for large N . We note that the standard wall superposition approximation entirely misses this behavior (Bhattacharya *et al.* 2005).

A better insight into the mechanisms underlying the above-illustrated qualitative features of the resistance matrix can be gained from the set of more detailed results for a chain of the length $N = 20$ plotted in figures 10 and 11. In these figures, we show the resistance coefficients

$$\bar{\zeta}_F^{\alpha\alpha}(i) = \zeta_0^{-1} \sum_{j=1}^N \zeta_{ij}^{\text{tt}\alpha\alpha}, \quad \alpha = x, y, z, \quad (7.16a)$$

and

$$\bar{\zeta}_T^{\beta\alpha}(i) = \frac{3}{2}(a\zeta_0)^{-1} \sum_{j=1}^N \zeta_{ij}^{\text{rt}\beta\alpha}, \quad \beta\alpha = zy, yz, \quad (7.16b)$$

representing the normalized applied force and torque

$$\mathcal{F}_i = \hat{\mathbf{e}}_\alpha \bar{\zeta}_F^{\alpha\alpha}(i), \quad \mathcal{T}_i = \hat{\mathbf{e}}_\beta \bar{\zeta}_T^{\beta\alpha}(i) \quad (7.17a, b)$$

acting on particle i in a chain moving in the direction α with a unit velocity. By symmetry,

the forces act only in the direction of the chain motion, and the only nonzero torque coefficients are those listed in equation (7.16b).

According to the results shown in figure 10 for the motion in the x direction, the forces acting on the first and the last particle in the chain are larger than the forces acting on the particles in the chain interior. This behavior is similar for chains in the unbounded and the wall-bounded regions. The forces are smaller for long chains, because the particles collectively drag the fluid in the direction of the chain velocity. This mechanism is diminished, but not eliminated by the wall presence.

In an unbounded space, the force distribution in a chain moving in the transverse direction y is qualitatively similar to the distribution for the longitudinal motion discussed above. In the wall-bounded region the results are, however, considerably different: the forces near the center of the chain are much larger than the forces near the chain ends. This behavior, clearly seen in figure 10 for $H/2a \lesssim 2$, stems from the conservation of the fluid volume. The chain moving in the transverse direction acts like a piston pushing fluid along the space between the walls, thus producing a pressure-driven flow decaying on the lengthscale $l = 2aN$. The pressure increases linearly with the chain length until it is large enough to push the fluid back through the gap between the walls and the particles. At this point, the pressure becomes independent of N . The pressure produced by this mechanism is responsible for the large resistance coefficient $\bar{\zeta}_C^{yy}$ of long chains in transverse motion between closely spaced walls, as shown in figure 9.

For a chain moving in the direction z (normal to the walls) in a system with a small value of the wall-particle gap ϵ , the resistance coefficients $\bar{\zeta}_C^{zz}$ are dominated by the lubrication forces between the walls and the individual particles. The coefficients $\bar{\zeta}_C^{zz}$ are the smallest for the spheres at the chain ends, as seen in figure 10, unlike for chains in the infinite space. This behavior stems from the presence of the geometrical constraints—the resistance is smaller where there is more room for the fluid to escape from the gaps between the walls and the particles.

The geometrical-parameter dependence of the torque acting on individual spheres in a translating chain is less varied, as illustrated in figure 11. In all configurations considered, we find that the torque on the interior spheres is much smaller than the torque at the chain ends. An interesting feature is the sign change of the torque acting on the particle $i = 2$ for the coefficient $\bar{\zeta}_T^{yz}$.

8. Conclusions

Many-body hydrodynamic interactions in suspensions of spherical particles confined between two parallel planar walls have been studied here theoretically and numerically. Our primary theoretical result is a set of compact expressions for the multipolar matrix elements of the Green's integral operator for Stokes flow in the space between the walls. The matrix elements are given in the form of lateral Fourier integrals of products of several simple matrices.

Our expressions have been used to develop an algorithm for evaluating many-particle hydrodynamic friction and mobility matrices in a wall-bounded suspension. The algorithm involves solving a set of linear equations for the multipolar moments of the force distributions induced on the particles. The resulting friction matrix is corrected for the lubrication forces by using a superposition of particle-particle and particle-wall contributions. Our algorithm yields highly accurate results—for example, the results presented in this paper have been obtained with an accuracy better than 1%. We note that at each truncation of the force-multipole expansion the boundary conditions at the walls

are exactly satisfied. This feature is essential for obtaining a proper far-field behavior of the friction matrix, including the strong backflow effects seen for rigid arrays of spheres.

Our numerical algorithm has been used to evaluate the hydrodynamic resistance matrix for a single particle, a pair of particles, and a system of many particles confined between two planar walls. The problem of hydrodynamic interactions in the two-wall geometry involves several characteristic lengthscales: the particle radius a , the wall-to-wall distance H , and the lateral distance between the particles ρ . For $\rho \ll H$ the interactions between particles are similar to those in the infinite space. For $\rho \approx H$ the crossover occurs to a quasi-two-dimensional behavior in the regime $\rho \gg H$.

In the quasi-two-dimensional domain the vertical components of the mutual pair resistance matrix decay exponentially, and the lateral components behave as $O(\rho^{-2})$. Moreover, the sign of the transverse component of the resistance matrix is opposite to the sign of this component for a pair of particles in infinite space. As discussed here and in our recent paper (Bhattacharya *et al.* 2005), this behavior can be explained using the asymptotic Hele-Shaw (lubrication) form of the far-field flow produced by a moving particle.

The crossover behavior is particularly pronounced for rigid arrays of spheres arranged along a line parallel to the walls. In the regime $a \ll l \ll H$, where l is the chain length, the hydrodynamic friction force per particle decreases as $(\log l)^{-1}$ for large l , similar to the behavior in the infinite space. In contrast, for $l \gg H$ the longitudinal component of the friction tensor (per particle) and the component normal to the walls tend to constant values. Moreover, for small particle-wall gaps, the transverse component (normal to the chain but parallel to the walls) increases linearly with the chain length before it saturates at a value that is much higher than the corresponding value for the longitudinal motion.

As discussed in our recent paper (Bhattacharya *et al.* 2005), the standard wall-superposition approximation is insufficient for many problems. The resistance matrix in such an approximation is composed from two single-wall contributions. In particular, the superposition approximation yields a wrong sign of the transverse component of the mutual pair resistance matrix and a wrong far-field behavior of all components of this matrix. The approximation also fails to reproduce the striking increase with the number of particles for the transverse resistance coefficient of linear arrays of spheres.

The numerical efficiency of our method can be substantially improved by combining our Cartesian representation of the wall contribution to the Green's matrix with the asymptotic far-field expressions for this quantity. The asymptotic expressions which we have recently derived can be expressed in terms of multipolar solutions of Laplace's equation for two-dimensional pressure field corresponding to the lubrication flow in the space between the walls. These expressions do not involve Fourier integrals, and they can be implemented in numerical algorithms for periodic systems and in accelerated PPPM or fast-multipole algorithms.

S. B. would like to acknowledge the support by NSF grant CTS-0201131. E. W. was supported by NASA grant NAG3-2704 and in part by KBN grant No. 5T07C 035 22. J. B. was supported by NSF grant cts-s0348175 and by Hellman Foundation.

Appendix A. Spherical basis

The spherical basis of Stokes flows $\mathbf{v}_{lm\sigma}^{\pm}$ and the reciprocal basis fields $\mathbf{w}_{lm\sigma}^{\pm}$ used in the present paper are normalized differently than the corresponding basis fields $\mathbf{v}_{lm\sigma}^{\pm(\text{CFS})}$ and $\mathbf{w}_{lm\sigma}^{\pm(\text{CFS})}$ introduced by Cichocki *et al.* (1988). The relations between these sets of

basis functions are as follows:

$$\mathbf{v}_{lm\sigma}^-(\mathbf{r}) = N_{l\sigma}^{-1} n_{lm}^{-1} \mathbf{v}_{lm\sigma}^{-(\text{CFS})}(\mathbf{r}), \quad \mathbf{v}_{lm\sigma}^+(\mathbf{r}) = N_{l\sigma} n_{lm}^{-1} \mathbf{v}_{lm\sigma}^{+(\text{CFS})}(\mathbf{r}), \quad (\text{A } 1a)$$

$$\mathbf{w}_{lm\sigma}^-(\mathbf{r}) = N_{l\sigma} n_{lm} r \mathbf{w}_{lm\sigma}^{-(\text{CFS})}(\mathbf{r}), \quad \mathbf{w}_{lm\sigma}^+(\mathbf{r}) = N_{l\sigma}^{-1} n_{lm} r \mathbf{w}_{lm\sigma}^{+(\text{CFS})}(\mathbf{r}), \quad (\text{A } 1b)$$

where

$$N_{l0} = 1, \quad N_{l1} = -(l+1)^{-1}, \quad N_{l2} = l[(l+1)(2l+1)(2l+3)]^{-1}, \quad (\text{A } 2)$$

and

$$n_{lm} = \left[\frac{4\pi}{2l+1} \frac{(l+m)!}{(l-m)!} \right]^{1/2}. \quad (\text{A } 3)$$

Below we list the explicit expressions for the angular coefficients $\mathbf{V}_{lm\sigma}^\pm(\theta, \phi)$ for spherical basis fields (3.1) in our present normalization,

$$\mathbf{V}_{lm0}^- = \frac{1}{(2l+1)^2} \left[\frac{l+1}{l(2l-1)} \alpha_l \mathbf{Y}_{l, l-1, m} - \frac{1}{2} \mathbf{Y}_{l, l+1, m} \right], \quad (\text{A } 4a)$$

$$\mathbf{V}_{lm1}^- = \frac{i}{l+1} \gamma_l \mathbf{Y}_{l, l, m}, \quad (\text{A } 4b)$$

$$\mathbf{V}_{lm2}^- = \beta_l \mathbf{Y}_{l, l+1, m}, \quad (\text{A } 4c)$$

and

$$\mathbf{V}_{lm0}^+ = \alpha_l \mathbf{Y}_{l, l-1, m}, \quad (\text{A } 5a)$$

$$\mathbf{V}_{lm1}^+ = \frac{i}{l+1} \gamma_l \mathbf{Y}_{l, l, m}, \quad (\text{A } 5b)$$

$$\mathbf{V}_{lm2}^+ = \frac{l}{2(2l+1)} \alpha_l \mathbf{Y}_{l, l-1, m} + \frac{l}{(l+1)(2l+1)(2l+3)} \beta_l \mathbf{Y}_{l, l+1, m}, \quad (\text{A } 5c)$$

where

$$\mathbf{Y}_{l, l-1, m}(\hat{\mathbf{r}}) = \alpha_l^{-1} r^{-l+1} \nabla [r^l Y_{lm}(\hat{\mathbf{r}})], \quad (\text{A } 6a)$$

$$\mathbf{Y}_{l, l+1, m}(\hat{\mathbf{r}}) = \beta_l^{-1} r^{l+2} \nabla [r^{-(l+1)} Y_{lm}(\hat{\mathbf{r}})], \quad (\text{A } 6b)$$

$$\mathbf{Y}_{l, l, m}(\hat{\mathbf{r}}) = \gamma_l^{-1} \mathbf{r} \times \nabla_s Y_{lm}(\hat{\mathbf{r}}) \quad (\text{A } 6c)$$

are the normalized vector spherical harmonics, as defined by Edmonds (1960). Here

$$Y_{lm}(\hat{\mathbf{r}}) = n_{lm}^{-1} (-1)^m P_l^m(\cos \theta) e^{im\varphi} \quad (\text{A } 7)$$

are the normalized scalar spherical harmonics, and

$$\alpha_l = [l(2l+1)]^{1/2}, \quad \beta_l = [(l+1)(2l+1)]^{1/2}, \quad \gamma_l = -i[l(l+1)]^{1/2}. \quad (\text{A } 8)$$

Appendix B. Transformation vectors \mathbf{X}^t and \mathbf{X}^r

The resistance matrix (2.1) is obtained from the solution

$$\mathbf{f}_i(lm) = \sum_{j=1}^N \sum_{l'm'} \mathbf{F}_{ij}(lm | l'm') \cdot \mathbf{c}_j(l'm') \quad (\text{B } 1)$$

of the force-multipole equation (3.8) by projecting the generalized friction matrix $\mathbf{F} = \mathbf{M}^{-1}$ onto the subspaces corresponding to the rigid-body motion of the particle j and the total force and torque of the induced-force distribution on particle i . As shown in Ref. I, the projection can be expressed in the form

$$\zeta_{ij}^{AB} = \sum_{lm\sigma} \sum_{l'm'\sigma'} \mathbf{X}(A | lm\sigma) F_{ij}(lm\sigma | l'm'\sigma') \mathbf{X}(l'm'\sigma' | B), \quad (\text{B } 2)$$

where $A, B = t, r$. Here $\mathbf{X}(A | lm\sigma)$ and $\mathbf{X}(l'm'\sigma' | B)$ are the projection vectors defined by the equations

$$\mathbf{X}(t | lm\sigma) = \delta_{l1} \delta_{\sigma 0} \tilde{\mathbf{X}}^t(m), \quad \mathbf{X}(r | lm\sigma) = \delta_{l1} \delta_{\sigma 1} \tilde{\mathbf{X}}^r(m), \quad (\text{B } 3)$$

$$\tilde{\mathbf{X}}^t(-1) = (\frac{2}{3}\pi)^{1/2} \begin{bmatrix} 1 \\ -i \\ 0 \end{bmatrix}, \quad \tilde{\mathbf{X}}^t(0) = (\frac{2}{3}\pi)^{1/2} \begin{bmatrix} 0 \\ 0 \\ \sqrt{2} \end{bmatrix}, \quad \tilde{\mathbf{X}}^t(1) = (\frac{2}{3}\pi)^{1/2} \begin{bmatrix} -1 \\ -i \\ 0 \end{bmatrix}, \quad (\text{B } 4)$$

$$\tilde{\mathbf{X}}^r(m) = -2i\tilde{\mathbf{X}}^t(m), \quad m = -1, 0, 1, \quad (\text{B } 5)$$

and

$$\mathbf{X}(lm\sigma | A) = \mathbf{X}^*(A | lm\sigma), \quad A = t, r. \quad (\text{B } 6)$$

Appendix C. Cartesian basis fields

The Fourier coefficients $\mathbf{V}_{\mathbf{k}\sigma}^{\pm}(z)$ in the expression (4.1) for the Cartesian basis fields are given by the expressions

$$\mathbf{V}_{\mathbf{k}0}^{-}(z) = (32\pi^2)^{-1/2} \left[i(1 - 2kz)\hat{\mathbf{k}} + (1 + 2kz)\hat{\mathbf{e}}_z \right] k^{-1/2}, \quad (\text{C } 1a)$$

$$\mathbf{V}_{\mathbf{k}1}^{-}(z) = (8\pi^2)^{-1/2} (\hat{\mathbf{k}} \times \hat{\mathbf{e}}_z) k^{-1/2}, \quad (\text{C } 1b)$$

$$\mathbf{V}_{\mathbf{k}2}^{-}(z) = (32\pi^2)^{-1/2} (i\hat{\mathbf{k}} - \hat{\mathbf{e}}_z) k^{-1/2}, \quad (\text{C } 1c)$$

and

$$\mathbf{V}_{\mathbf{k}0}^{+}(z) = (32\pi^2)^{-1/2} (i\hat{\mathbf{k}} + \hat{\mathbf{e}}_z) k^{-1/2}, \quad (\text{C } 2a)$$

$$\mathbf{V}_{\mathbf{k}1}^{+}(z) = (8\pi^2)^{-1/2} (\hat{\mathbf{k}} \times \hat{\mathbf{e}}_z) k^{-1/2}, \quad (\text{C } 2b)$$

$$\mathbf{V}_{\mathbf{k}2}^{+}(z) = (32\pi^2)^{-1/2} \left[i(1 + 2kz)\hat{\mathbf{k}} - (1 - 2kz)\hat{\mathbf{e}}_z \right] k^{-1/2}, \quad (\text{C } 2c)$$

where $\hat{\mathbf{k}} = \mathbf{k}/k$. The corresponding pressure fields are

$$p_{\mathbf{k}0}^{-}(\mathbf{r}) = (2\pi^2)^{-1/2} \eta k^{1/2} e^{i\mathbf{k} \cdot \boldsymbol{\rho} - kz}, \quad p_{\mathbf{k}2}^{+}(\mathbf{r}) = (2\pi^2)^{-1/2} \eta k^{1/2} e^{i\mathbf{k} \cdot \boldsymbol{\rho} + kz}, \quad (\text{C } 3)$$

and

$$p_{\mathbf{k}1}^{-}(\mathbf{r}) = p_{\mathbf{k}2}^{-}(\mathbf{r}) = p_{\mathbf{k}0}^{+}(\mathbf{r}) = p_{\mathbf{k}1}^{+}(\mathbf{r}) = 0. \quad (\text{C } 4)$$

- BHATTACHARYA, S. & BŁAWZDZIEWICZ, J. 2002*a* Image system for Stokes-flow singularity between two parallel planar walls. *J. Math. Phys.* **43**, 5720–31.
- BHATTACHARYA, S. & BŁAWZDZIEWICZ, J. 2002*b* Motion of a rigid sphere between two parallel walls AICHE Annual Meeting, Indianapolis, 3–8 November 2002.
- BHATTACHARYA, S., BŁAWZDZIEWICZ, J. & WAJNRYB, E. 2005 Many-particle hydrodynamic interactions in parallel-wall geometry: Cartesian-representation method. *Physica A* **in review**, xxxx.
- BŁAWZDZIEWICZ, J., CRISTINI, V. & LOEWENBERG, M. 1999 Stokes flow in the presence of a planar interface covered with incompressible surfactant. *Phys. Fluids* **11**, 251–258.
- BŁAWZDZIEWICZ, J. & WAJNRYB, E. 2003 Hydrodynamics of particle-stabilized thin liquid film AICHE Annual Meeting, San Francisco, 16–21 November 2003.
- BŁAWZDZIEWICZ, J., WAJNRYB, E., GIVEN, J. A. & HUBBARD, J. B. 2005 Sharp scalar and tensor bounds on the hydrodynamic friction and mobility of arbitrarily shaped bodies in Stokes flow. *Phys. Fluids* **xxx**, xxx.
- BŁAWZDZIEWICZ, J., WAJNRYB, E. & LOEWENBERG, M. 1999 Hydrodynamic interactions and collision efficiencies of spherical drops covered with an incompressible surfactant film. *J. Fluid Mech.* **395**, 29–59.
- CARBAJAL-TINOCO, M. D., CRUZ DE LEÓN, G. & ARAUZ-LARA, J. L. 1997 Brownian motion in quasibidimensional colloidal suspensions. *Phys. Rev. E* **56**, 6962–9.
- CICHOCKI, B., EKIEL-JEŻEWSKA, M. L., NAGELE, G. & WAJNRYB, E. 2004 Motion of spheres along fluid–gas interface. *J. Chem. Phys.* **121**, 2305–16.
- CICHOCKI, B. & FELDERHOF, B. U. 1994 Self-diffusion of interacting Brownian particles in a plane. *J. Phys: Condens. Matter* **6**, 7287–302.
- CICHOCKI, B., FELDERHOF, B. U., HINSEN, K., WAJNRYB, E. & BŁAWZDZIEWICZ, J. 1994 Friction and mobility of many spheres in Stokes flow. *J. Chem. Phys.* **100**, 3780–3790.
- CICHOCKI, B., FELDERHOF, B. U. & SCHMITZ, R. 1988 Hydrodynamic interactions between two spherical particles. *PhysicoChem. Hyd.* **10**, 383–403.
- CICHOCKI, B. & JONES, R. B. 1998 Image representation of a spherical particle near a hard wall. *Physica A* **258**, 273–302.
- CICHOCKI, B., JONES, R. B., KUTTEH, R. & WAJNRYB, E. 2000 Friction and mobility for colloidal spheres in Stokes flow near a boundary: The multipole method and applications. *J. Chem. Phys.* **112**, 2548–61.
- COX, R. G. & BRENNER, H. 1967 Effect of finite boundaries on Stokes resistance of an arbitrary particle .3. translation and rotation. *J. Fluid Mech.* **28**, 391.
- DURLOFSKY, L., BRADY, J. F. & BOSSIS, G. 1987 Dynamic simulation of hydrodynamically interacting particles. *J. Fluid Mech.* **180**, 21–49.
- DURLOFSKY, L. J. & BRADY, J. F. 1989 Dynamic simulation of bounded suspensions of hydrodynamically interacting particles. *J. Fluid. Mech.* **200**, 39–67.
- EDMONDS, A. R. 1960 *Angular Momentum in Quantum Mechanics*. Princeton: Princeton University Press.
- FELDERHOF, B. U. 1976 Force density induced on a sphere in linear hydrodynamics. II. Moving sphere, mixed boundary conditions. *Physica A* **84**, 569–576.
- FELDERHOF, B. U. & JONES, R. B. 1989 Displacement theorems for spherical solutions of the linear Navier-Stokes equations. *J. Math. Phys.* **30**, 339–42.
- GANATOS, P., PFEFFER, R. & WEINBAUM, S. 1980*a* A strong interaction theory for the creeping motion of a sphere between plane parallel boundaries. Part 2. Parallel motion. *J. Fluid Mech.* **99**, 755–83.
- GANATOS, P., WEINBAUM, S. & PFEFFER, R. 1980*b* A strong interaction theory for the creeping motion of a sphere between plane parallel boundaries. Part 1. Perpendicular motion. *J. Fluid Mech.* **99**, 739–53.
- JONES, R. B. 2004 Spherical particle in Poiseuille flow between planar walls. *J. Chem. Phys.* **121**, 483–500.
- JONES, R. B. & SCHMITZ, R. 1988 Mobility matrix for arbitrary spherical particles in solution. *Physica A* **149**, 373–394.
- KIM, S. & KARRILA, S. J. 1991 *Microhydrodynamics: Principles and Selected Applications*. London: Butterworth-Heinemann.

- LADD, A. J. C. 1988 Hydrodynamic interactions in suspensions of spherical particles. *J. Chem. Phys.* **88**, 5051.
- LANÇON, P., BATROUNI, G., LOBRY, L. & OSTROWSKY, N. 2001 Drift without flux: Brownian walker with a space-dependent diffusion coefficient. *Europhys. Lett.* **54**, 28–34.
- LIN, K. H., CROCKER, J. C., PRASAD, V., SCHOFIELD, A., WEITZ, D. A., LUBENSKY, T. & YODH, A. 2000 Entropically driven colloidal crystallization on patterned surfaces. *Phys. Rev. Lett.* **85**, 1770.
- LIRON, N. & MOCHON, S. 1976 Stokes flow for a stokeslet between two parallel flat plates. *J. Engineering Math.* **10**, 287–303.
- LYON, M. K. & LEAL, L. G. 1998 An experimental study of the motion of concentrated suspensions in two-dimensional channel flow. Part 1. Monodisperse systems. *J. Fluid Mech.* **363**, 25–56.
- MARCUS, A. H. & RICE, S. A. 1997 Phase transitions in a confined quasi-two-dimensional suspension. *Phys. Rev. E* **55**, 637–56.
- MARCUS, A. H., SCHOFIELD, J. & RICE, S. A. 1999 Experimental observations of non-Gaussian behavior and stringlike cooperative dynamics in concentrated quasi-two-dimensional colloidal liquids. *Phys. Rev. E* **60**, 5725–36.
- MAZUR, P. & BEDEAUX, D. 1974 A generalization of Faxén’s theorem to nonsteady motion of a sphere through an incompressible fluid in arbitrary flow. *Physica* **76**, 235–46.
- MORRIS, J. F. & BRADY, J. F. 1998 Pressure-driven flow of a suspension: Buoyancy effects. *Int. J. Multiphase Flow* **24**, 105–30.
- NOTT, P. & BRADY, J. 1994 Pressure-driven flow of suspensions—simulation and theory. *J. Fluid Mech.* **275**, 157–199.
- PESCHÉ, R. & NÄGELE, G. 2000 Stokesian dynamics study of quasi-two-dimensional suspensions confined between two parallel walls. *Phys. Rev. E* **62**, 5432–43.
- RINN, B., ZAHN, K., MAASS, P. & MARET, G. 1999 Influence of hydrodynamic interactions on the dynamics of long-range interacting colloidal particles. *Europhys. Lett.* **46**, 537–41.
- SANTANA-SOLANO, J. & ARAUZ-LARA, J. L. 2001 Hydrodynamic interactions in quasi-two-dimensional colloidal suspensions. *Phys. Rev. Lett.* **87**, 038302.
- SEELIG, E. W., TANG, B., YAMILOV, A., CAO, H. & CHANG, R. P. H. 2002 Self-assembled 3D photonic crystals from ZnO colloidal spheres. *Mater. Chem. Phys.* **80**, 257–63.
- SETHUMADHAVAN, G. N., NIKOLOV, A. D. & WASAN, D. T. 2001 Stability of liquid films containing monodisperse colloidal particles. *J. Colloid Interface Sci.* **240**, 105–12.
- SIEROU, A. & BRADY, J. F. 2001 Accelerated Stokesian dynamics simulations. *J. Fluid Mech.* **448**, 115–46.
- STABEN, M. E., ZINCHENKO, A. Z. & DAVIS, R. H. 2003 Motion of a particle between two parallel plane walls in low-Reynolds-number Poiseuille flow. *Phys. Fluids*. **15**, 1711–33.
- STANCIK, E. J. & HAWKINSON, A. L. 2003 Dynamic transitions and oscillatory melting of a two-dimensional crystal subjected to shear flow. *J. Rheol.* **48**, 159–73.
- SUBRAMANIAN, G., MANOHARAN, V. N., THORNE, J. D. & PINE, D. J. 1999 Ordered macroporous materials by colloidal assembly: A possible route to photonic bandgap materials. *Adv. Mater.* **11**, 1261–1265.
- WEI, Q.-H., BECHINGER, C. & LEIDERER, P. 2000 Single-file diffusion of colloids in one-dimensional channels. *Science* **287**, 625–7.
- ZAHN, K., MÉNDEZ-ALCARAZ, J. M. & MARET, G. 1997 Hydrodynamic interactions may enhance the self-diffusion of colloidal particles. *Phys. Rev. Lett.* **79**, 175–8.